Finite-volumes Based FDTD Material Dispersion Modeling

by

Neeti Prakash Sonth

B.Tech, Visvesvaraya National Institute of Technology Nagpur 2014

A thesis submitted to the

Faculty of the Graduate School of the

University of Colorado in partial fulfillment

of the requirements for the degree of

Master of Science

Department of Electrical Engineering

2018

This thesis entitled:
Finite-volumes Based FDTD Material Dispersion Modeling
written by Neeti Prakash Sonth
has been approved for the Department of Electrical Engineering

_____
Prof. Melinda Piket-May

_____
Prof. Mohammed Hadi

Date _____

The final copy of this thesis has been examined by the signatories, and we find that both the content and the form meet acceptable presentation standards of scholarly work in the above-mentioned discipline.

Sonth, Neeti Prakash (M.S., Electrical Engineering)

Finite-volumes Based FDTD Material Dispersion Modeling

Thesis directed by Prof. Melinda Piket-May/Prof. Mohammed Hadi

Abstract

The conventional FDTD, based on second-order central difference formula, is useful only so long as the electrical size of the structure is small. Phase error accumulates in the field calculations as the dimensions of the numerical FDTD lattice become larger. The Finite Volumes-Based 3-D second-order in time, fourth-order in space (FV24) modeling is highly capable of controlling such phase errors. Therefore, it is suitable for electrically large problems at coarse grid resolutions.

This work models the frequency dependence of material losses using an Auxiliary Differential Equation (ADE) technique. To account for material dispersion, the derivation of ADE is extended for FV24 by modifying the electric field update equations. A Multipole Debye model, which provides an auxiliary differential equation in time domain and produces a causal response, is used in the current analysis. This model, suitable for FDTD simulations, can simulate relative permittivity and conductivity of materials with high degree of accuracy over a wide bandwidth.

For the present study, a simple dielectric scatterer and breast tumor model are used as the problem space. The planewave excitation is provided using the total field/scattered field-based leakage free technique. The FV24 algorithm, being accurate even at coarse discretizations, provides excellent wideband performance. Keeping low number of cells per wavelength provides a substantial decrease in floating-point operations per wavelength, enabling faster computation. This fact allows significant reduction in memory usage. This feature of FV24 renders it relatively less expensive than FDTD to model three-dimensional (3-D) problems that are hundreds of wavelengths large. A comparison of accuracy and performance in terms of memory usage and simulation time of conventional FDTD versus FV24 will be presented.

Acknowledgements

I would like to take the opportunity of showing profound respect to my advisor Prof. Melinda Piket-May, for giving me the opportunity to work in this thesis and for supervising it. I thank her for providing me with a congenial and friendly atmosphere to work. The guidance and assistance I have received from her during the entire course of my thesis work will help me in the long journey of my academic and professional career.

It is a great pleasure to acknowledge my deepest thanks and gratitude to Prof. Mohammed Hadi, for suggesting the topic of this thesis, and his kind supervision. The constructive criticism and timely support I received from him has been instrumental in the progress of my thesis work.

I would also like to extend my gratitude to Prof. Eric Bogatin for graciously agreeing to attend the thesis dissertion and providing me with some productive feedbacks. I thank Prof. Atef Elsherbeni for his generous advice and support during the study. His book '*The Finite Difference Time Domain Method for Electromagnetics: With MATLAB Simulations*' has been pivotal for this thesis. I thank the Ph.D student – Ravi Bollimuntha for his constant support in helping me with modeling and algorithms, helping me clearly understand the technical aspects and his patience towards my questions. I am also grateful to Alec Weiss, Hugo Stetz and Madhavi Rao for taking their time to help me with submitting jobs on Supercomputer. I am indebted to Aman Samaiyar, the Ph.D student for helping with the script for Summit. I would also like to thank the Research Computing Staff for their timely help with resolving my issues and answering my questions. I am thankful to Kevin Quillen, Lead Application Engineer at Ansys, for helping me with the breast tumor model in HFSS-IE. I would also like to thank Dharma Teja Paladugu, Software Engineer at Cadence Design Systems, for helping me with some concepts.

I would also like to thank Mr. Sunil Sumanth, my manager at Mentor Graphics and Priya VG, my peer at Mentor Graphics, for providing me encouragement and support throughout the semester.

I would like to thank Adam Sadoff, ECEE advisor, for providing information on thesis. I

thank the Almighty, my parents Mrs.M.Sonth and Mr.P.Sonth and my brother Master Akash Sonth for their love, constant motivation and support throughout my academic journey. I would like to give my special thanks to all my friends and colleagues.

Contents

Tables

Table

Figures

Figure

Chapter 1

Introduction and Background

Electromagnetics is the study of electrical and magnetic fields and their interaction. It is governed by Maxwell's Equations namely, Faraday's Law, Ampere's Circuital Law, and Gauss' Laws. Computational Electromagnetics is the process of modeling the interaction of electromagnetic fields with physical objects and the environment. Actual solution for realistic problems is complex and requires simplifying assumptions and/or numerical approximations. Computationally efficient approximations to Maxwell's equations are required to solve such problems. Solutions to Maxwell's equations using numerical approximations is known as the study of Computational Electromagnetics (CEM). These have innumerable applications such as, to calculate antenna performance, electromagnetic compatibility, radar cross section and electromagnetic wave propagation when not in free space. CEM is a numerical field-solving methodology, in which, differential equation (DE) or integral equations (IE) are solved. Different kinds of CEM methods are discussed in literature, such as, Method of Moments (MoM), Finite Element Method (FEM) and FDTD (finite Difference Time Domain). FEM and Mom are frequency domain approaches while FDTD is a time domain approach.

The work in this thesis focuses on their material dispersion modeling in dispersive objects using higher order FDTD method. In this introductory chapter, background information about the FDTD method, the update equations for three-dimensional structure, the procedure of FDTD implementation and relative merits and demerits of conventional FDTD are elaborated.

1.1 FDTD Implementation

Conventional FDTD, also simply known as FDTD is based on discretization of Electric and Magnetic fields from Maxwell's time-domain equations. Equations 1.1-1.4 show these equations

$$\nabla X H_v = \frac{\partial D_v}{\partial t} + J_v \quad (1.1)$$

$$\nabla X E_v = -\frac{\partial B_v}{\partial t} - M_v \quad (1.2)$$

$$\nabla . D_v = \rho_e \quad (1.3)$$

$$\nabla . B_v = \rho_m \quad (1.4)$$

Where E_v is the electric field strength vector in volts per meter, D_v is the electric displacement vector in coulombs per square meter, H_v is the magnetic field strength vector in amperes per meter, B_v is the magnetic flux density vector in webers per square meter, J_v is the electric current density vector in amperes per square meter, M_v is the magnetic current density vector in volts per square meter, ρ_e is the electric charge density in coulombs per cubic meter, and ρ_m is the magnetic charge density in webers per cubic meter.

For linear, isotropic and nondispersive materials, Maxwell's equations can be written as:

$$\nabla X H_v = \varepsilon \frac{\partial E_v}{\partial t} + \sigma^e + J_{iv} \quad (1.5)$$

$$\nabla X E_v = -\mu \frac{\partial H_v}{\partial t} - \sigma^m H_v - M_{iv} \quad (1.6)$$

Where the electric current density J_v is the sum of the conduction current density $J_{cv} = \sigma^e E_v$ and the impressed current density J_i is $J_v = J_{cv} + J_{iv}$. Similarly, for the magnetic current density, $M_v = M_{cv} + M_{iv}$ where $M_{cv} = \sigma^m H_v$. Here σ^e is the electric conductivity in siemens per meter, and σ^m is the magnetic conductivity in ohms per meter. The divergence equations 1.3-1.4 are incorporated in Maxwell's curl equations 1.5-1.6 where $D_v = \varepsilon E_v$ and

$B_v = \mu\, H_v$. ε is the permittivity μ is the permeability of the material. In free space,

$$\varepsilon = \varepsilon_0 = 8.854e^{-12} farad/meter \quad \text{and} \quad \mu = \mu_0 = 4\pi e^{-7} henry/meter$$

Equations 1.5-1.6 are the Maxwells' curl equations which can be written in the form of 6 Cartesian differential equation as below [1]:

$$\frac{\partial E_x}{\partial t} = \frac{1}{\varepsilon_x}\left(\frac{\partial H_z}{\partial y} - \frac{\partial H_y}{\partial z} - \sigma_x^e E_x - J_{ix}\right) \tag{1.7}$$

$$\frac{\partial E_y}{\partial t} = \frac{1}{\varepsilon_y}\left(\frac{\partial H_x}{\partial z} - \frac{\partial H_z}{\partial x} - \sigma_y^e E_y - J_{iy}\right) \tag{1.8}$$

$$\frac{\partial E_z}{\partial t} = \frac{1}{\varepsilon_z}\left(\frac{\partial H_y}{\partial x} - \frac{\partial H_x}{\partial y} - \sigma_z^e E_z - J_{iz}\right) \tag{1.9}$$

$$\frac{\partial H_x}{\partial t} = \frac{1}{\mu_x}\left(\frac{\partial E_y}{\partial z} - \frac{\partial E_z}{\partial y} - \sigma_x^m H_x - M_{ix}\right) \tag{1.10}$$

$$\frac{\partial H_y}{\partial t} = \frac{1}{\mu_y}\left(\frac{\partial E_z}{\partial x} - \frac{\partial E_x}{\partial z} - \sigma_y^m H_y - M_{iy}\right) \tag{1.11}$$

$$\frac{\partial H_z}{\partial t} = \frac{1}{\mu_z}\left(\frac{\partial E_x}{\partial y} - \frac{\partial E_y}{\partial x} - \sigma_z^m H_z - M_{iz}\right) \tag{1.12}$$

These are then decomposed into finite difference equations in discretized form for the FDTD computation of a problem. These equations can be represented in discrete form, both in space and time, employing the second-order accurate central difference formula [15].

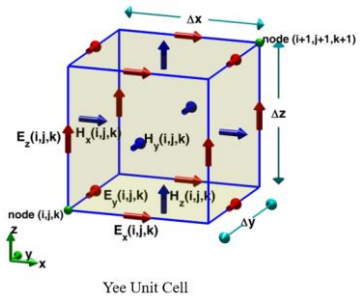

Figure 1.1: Arrangement of field components on a Yee cell indexed as (i, j, k).

The electric and magnetic field components are sampled at discrete positions both in time and space. The FDTD technique divides the three-dimensional problem geometry into cells to form a grid. Fig 1.1 shows the unit cell of an FDTD grid. This unit cell is called a Yee cell. Using rectangular Yee cells, a stepped or "staircase" approximation of the surface and internal geometry of the structure of interest is made with a space resolution set by the size of the unit cell. The electric field vector components are placed at the centers of the edges of the Yee cells and parallel to respective edges, and the magnetic field vector components are placed at the centers of the faces of the Yee cells and normal to respective faces. Each magnetic field vector is surrounded by four electric field vectors that are curling around the magnetic field vector, which simulates Faraday's law. Considering the neighboring cells of the FDTD grid, it would be seen that each electric field vector is surrounded by four magnetic field vectors that are curling around the electric field vector, which simulates Ampere's law.

For a time-sampling period Δt, the electric field components are calculated at integer time steps at time-instants 0, Δt, $2\Delta t$, and so on. The magnetic field components are calculated at half-integer time steps, and they are offset from each other by $\Delta t/2$. Thus, magnetic field components are sampled at time instants $(1/2)\Delta t$, $(1+(1/2))\Delta t$, and so on. The material parameters (permittivity, permeability, electric, and magnetic conductivities) are distributed over the FDTD grid and are associated with field components; therefore, they are indexed the same as their respective field components as shown in Fig 1.2 [15].

The derivatives in equations 1.7-1.12 are approximated by using central difference formula. For example, consider equation 1.7 which is the equation for temporal differential equation for E_x. Using central difference formula for space and time, $E_x(i, j, k)$ is considered as the center point. Time instant $(n+(1/2))\Delta t$ is considered as the center point in time. This is shown in equation 1.13. In equation 1.13, electric field term $E_x^{n+(1/2)}(i, j, k)$ at time instant

(n+1))Δt, can be written as the average of the terms at time instants (n+1)Δt and nΔt as shown in equation 1.14 [15].

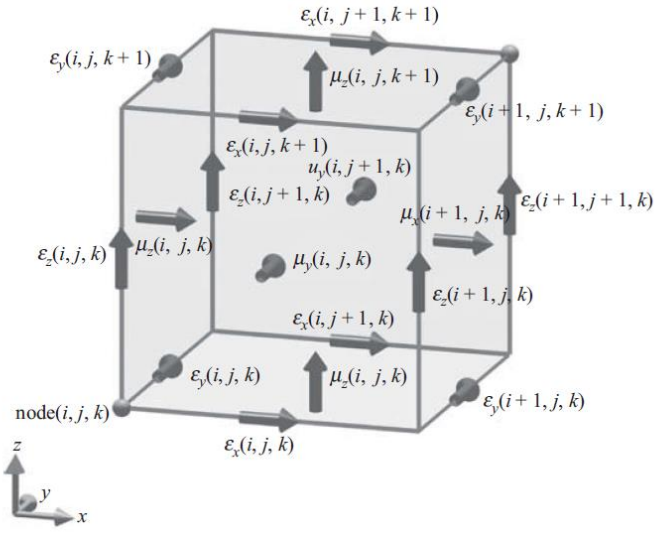

Figure 1.2: Material parameters indexed on a Yee cell

In these equations, the electric and magnetic currents would be considered as zero for this work. This is because, the region or problem space is considered source-free.

$$\frac{E_x^{n+1}(i,j,k)\ -E_x^n(i,j,k)}{\Delta t}=\frac{1}{\varepsilon_x(i,j,k)}\frac{H_z^{n+\frac{1}{2}}(i,j,k)-H_z^{n+\frac{1}{2}}(i,j-1,k)}{\Delta y}$$
$$-\ \frac{1}{\varepsilon_x(i,j,k)}\frac{H_y^{n+\frac{1}{2}}(i,j,k)-H_y^{n+\frac{1}{2}}(i,j,k-1)}{\Delta z}$$
$$-\ \frac{\sigma_x^e(i,j,k)}{\varepsilon_x(i,j,k)}\frac{E_x^{n+\frac{1}{2}}(i,j,k)}{1}-\frac{1}{\varepsilon_x(i,j,k)}\frac{J_{ix}^{n+\frac{1}{2}}(i,j,k)}{1} \qquad (1.13)$$

$$E_x^{n+\frac{1}{2}}(i,j,k)=\frac{E_x^{n+1}(i,j,k)+E_x^n(i,j,k)}{2} \qquad (1.14)$$

Using equations 1.13-1.14, and re-arrangement leads to equation 1.15 shown below.

$$E_x^{n+1}(i,j,k) = \frac{2\varepsilon_x(i,j,k) - \Delta t\sigma_x^e(i,j,k)}{2\varepsilon_x(i,j,k) + \Delta t\sigma_x^e(i,j,k)} E_x^n(i,j,k)$$

$$+ \frac{2\Delta t}{\left(2\varepsilon_x(i,j,k) + \Delta t\sigma_x^e(i,j,k)\right)\Delta y} (H_z^{n+\frac{1}{2}}(i,j,k)$$

$$- H_z^{n+\frac{1}{2}}(i,j-1,k))$$

$$- \frac{2\Delta t}{\left(2\varepsilon_x(i,j,k) + \Delta t\sigma_x^e(i,j,k)\right)\Delta z} (H_y^{n+\frac{1}{2}}(i,j,k)$$

$$- H_y^{n+\frac{1}{2}}(i,j,k-1))$$

$$- \frac{2\Delta t}{\left(2\varepsilon_x(i,j,k) + \Delta t\sigma_x^e(i,j,k)\right)} J_{ix}^{n+\frac{1}{2}}(i,j,k) \qquad (1.15)$$

From equation 1.15, it is seen that using past values of electric and magnetic field components, future values of electric field component can be calculated. For magnetic field given in equation 1.10, FDTD difference equation can be obtained considering the central point in time as nΔt. Thus, the final equation is as shown in equation 1.16 [15].

$$H_x^{n+\frac{1}{2}}(i,j,k) = \frac{2\mu_x(i,j,k) - \Delta t\sigma_x^m(i,j,k)}{2\mu_x(i,j,k) + \Delta t\sigma_x^m(i,j,k)} H_x^{n-\frac{1}{2}}(i,j,k)$$

$$+ \frac{2\Delta t}{\left(2\mu_x(i,j,k) + \Delta t\sigma_x^m(i,j,k)\right)\Delta z} (E_y^n(i,j,k+1)$$

$$- E_y^n(i,j,k))$$

$$- \frac{2\Delta t}{\left(2\mu_x(i,j,k) + \Delta t\sigma_x^m(i,j,k)\right)\Delta y} (E_z^n(i,j+1,k)$$

$$- E_z^n(i,j,k))$$

$$- \frac{2\Delta t}{\left(2\mu_x(i,j,k) + \Delta t\sigma_x^m(i,j,k)\right)} M_{ix}^n(i,j,k) \qquad (1.16)$$

Equations 1.15 and 1.16 are called the FDTD updating equations for $E_x^{n+1}(i,j,k)$ and $H_x^{n+(1/2)}(i,j,k)$ respectively. Using similar approach, updating equations can be obtained for $E_y^{n+1}(i,j,k)$, $E_z^{n+1}(i,j,k)$, $H_y^{n+(1/2)}(i,j,k)$ and $H_z^{n+(1/2)}(i,j,k)$.

Using finite differences, following six FDTD updating equations can be obtained for the six components of electromagnetic fields, as seen in equations 1.17-1.22 [1,15].

$$E_x^{n+1}(i,j,k) = C_{exe}(i,j,k)X\ E_x^n(i,j,k) + C_{exhz}(i,j,k)\mathrm{X}\ (H_z^{n+\frac{1}{2}}(i,j,k) - H_z^{n+\frac{1}{2}}(i,j-1,k)) + C_{exhy}(i,j,k)\mathrm{X}\ (H_y^{n+\frac{1}{2}}(i,j,k) - H_y^{n+\frac{1}{2}}(i,j,k-1)) \quad (1.17)$$

In the above equation, coefficient terms are defined as shown in equation 1.18 [15]:

$$C_{exe}(i,j,k) = \frac{2\varepsilon_x(i,j,k) - \Delta t\sigma_x^e(i,j,k)}{2\varepsilon_x(i,j,k) + \Delta t\sigma_x^e(i,j,k)}$$

$$C_{exhz}(i,j,k) = \frac{2\Delta t}{\left(2\varepsilon_x(i,j,k) + \Delta t\sigma_x^e(i,j,k)\right)\Delta y}$$

$$C_{exhy}(i,j,k) = -\frac{2\Delta t}{\left(2\varepsilon_x(i,j,k) + \Delta t\sigma_x^e(i,j,k)\right)\Delta z} \quad (1.18)$$

Similarly,

$$E_y^{n+1}(i,j,k) = C_{eye}(i,j,k)X\ E_y^n(i,j,k) + C_{eyhx}(i,j,k)\mathrm{X}(\ H_x^{n+\frac{1}{2}}(i,j,k) - H_x^{n+\frac{1}{2}}(i,j,k-1)) + C_{eyhz}(i,j,k)\mathrm{X}\ (H_z^{n+\frac{1}{2}}(i,j,k) - H_z^{n+\frac{1}{2}}(i-1,j,k)) \quad (1.19)$$

where

$$C_{eye}(i,j,k) = \frac{2\varepsilon_y(i,j,k) - \Delta t\sigma_y^e(i,j,k)}{2\varepsilon_y(i,j,k) + \Delta t\sigma_y^e(i,j,k)}$$

$$C_{exhx}(i,j,k) = \frac{2\Delta t}{\left(2\varepsilon_y(i,j,k) + \Delta t\sigma_y^e(i,j,k)\right)\Delta z}$$

$$C_{eyhz}(i,j,k) = -\frac{2\Delta t}{\left(2\varepsilon_y(i,j,k) + \Delta t\sigma_y^e(i,j,k)\right)\Delta x} \quad (1.20)$$

And

$$E_z^{n+1}(i,j,k) = C_{eze}(i,j,k)X\ E_z^n(i,j,k) + C_{ezhy}(i,j,k)\mathrm{X}\ (H_y^{n+\frac{1}{2}}(i,j,k) - H_y^{n+\frac{1}{2}}(i-1,j,k)) + C_{ezhx}(i,j,k)\mathrm{X}\ (H_x^{n+\frac{1}{2}}(i,j,k) - H_x^{n+\frac{1}{2}}(i,j-1,k)) \quad (1.21)$$

where

$$C_{eze}(i,j,k) = \frac{2\varepsilon_z(i,j,k) - \Delta t\sigma_z^e(i,j,k)}{2\varepsilon_z(i,j,k) + \Delta t\sigma_z^e(i,j,k)}$$

$$C_{ezhy}(i,j,k) = \frac{2\Delta t}{\left(2\varepsilon_z(i,j,k) + \Delta t\sigma_z^e(i,j,k)\right)\Delta x}$$

$$C_{ezhx}(i,j,k) = -\frac{2\Delta t}{\left(2\varepsilon_z(i,j,k) + \Delta t\sigma_z^e(i,j,k)\right)\Delta y} \quad (1.22)$$

The magnetic field update equations along with their corresponding coefficients are shown in 1.23-1.28 [15].

$$H_x^{n+\frac{1}{2}}(i,j,k) = C_{hxh}(i,j,k)X\ H_x^{n-\frac{1}{2}}(i,j,k) + C_{hxey}(i,j,k)X\ (E_y^n(i,j,k+1) - E_y^n(i,j,k)) + C_{hxez}(i,j,k)(E_z^n(i,j+1,k) - E_z^n(i,j,k)) \quad (1.23)$$

Where

$$C_{hxh}(i,j,k) = \frac{2\mu_x(i,j,k) - \Delta t\sigma_x^m(i,j,k)}{2\mu_x(i,j,k) + \Delta t\sigma_x^m(i,j,k)}$$

$$C_{hxey}(i,j,k) = \frac{2\Delta t}{\left(2\mu_x(i,j,k) + \Delta t\sigma_x^m(i,j,k)\right)\Delta z}$$

$$C_{hxez}(i,j,k) = -\frac{2\Delta t}{\left(2\mu_x(i,j,k)+\Delta t\sigma_x^m(i,j,k)\right)\Delta y} \tag{1.24}$$

$$H_y^{n+\frac{1}{2}}(i,j,k) = C_{hyh}(i,j,k)X\, H_y^{n-\frac{1}{2}}(i,j,k) + C_{hyez}(i,j,k)X\,(E_z^n(i+1,j,k) - E_z^n(i,j,k)) + C_{hyex}(i,j,k)(E_x^n(i,j,k+1) - E_x^n(i,j,k)) \tag{1.25}$$

Where

$$C_{hyh}(i,j,k) = \frac{2\mu_y(i,j,k) - \Delta t\sigma_y^m(i,j,k)}{2\mu_y(i,j,k) + \Delta t\sigma_y^m(i,j,k)}$$

$$C_{hyez}(i,j,k) = \frac{2\Delta t}{\left(2\mu_y(i,j,k) + \Delta t\sigma_y^m(i,j,k)\right)\Delta x}$$

$$C_{hyex}(i,j,k) = -\frac{2\Delta t}{\left(2\mu_y(i,j,k)+\Delta t\sigma_y^m(i,j,k)\right)\Delta z} \tag{1.26}$$

And

$$H_z^{n+\frac{1}{2}}(i,j,k) = C_{hzh}(i,j,k)X\, H_z^{n-\frac{1}{2}}(i,j,k) + C_{hzex}(i,j,k)X\,(E_x^n(i,j+1,k) - E_x^n(i,j,k)) + C_{hzey}(i,j,k)(E_y^n(i+1,j,k) - E_y^n(i,j,k)) \tag{1.27}$$

Where

$$C_{hzh}(i,j,k) = \frac{2\mu_z(i,j,k) - \Delta t\sigma_z^m(i,j,k)}{2\mu_z(i,j,k) + \Delta t\sigma_z^m(i,j,k)}$$

$$C_{hzex}(i,j,k) = \frac{2\Delta t}{\left(2\mu_z(i,j,k) + \Delta t\sigma_z^m(i,j,k)\right)\Delta y}$$

$$C_{hzey}(i,j,k) = -\frac{2\Delta t}{\left(2\mu_z(i,j,k)+\Delta t\sigma_z^m(i,j,k)\right)\Delta x} \quad (1.28)$$

Using the above updating equations, time-marching loop is formed. Mathworks Matlab tool

is used or computation. Thus, these equations are solved iteratively for the number of time-steps of interest. The time-marching algorithm [15] sets up the problem space (sources, material types) and initiates the parameters used in FDTD computation. The coefficient terms for electric and magnetic fields are calculated and stored in an array. The electric and magnetic field components are initialized to zeros. On setting up proper boundary space, the magnetic and electric field components

are updated.

In this thesis, the region where the electric and magnetic fields are computed is considered

as source-free. Therefore, J_{ix}, J_{iy}, J_{iz}, M_{ix}, M_{iy} and M_{iz} terms are zero and hence, their corresponding coefficients are not required. The time-step for FDTD computation is taken according to below formula:

$$dt = courant\_factor*h/(c_o*sqrt(3)) \quad (1.29)$$

where courant_factor is a stability criterion which represents the Courant-Friedrichs-Lewy (CFL) condition [16] for the FDTD method. For this thesis, the following values are taken for parameters in equation 1.29.

c_o =3e-8 m/s represents the speed of light in vacuum.

h represents the spacial distance or resolution of unit cell.

courant_factor=0.9

For S22, resolution of R=20, which is termed as S2220 and R=40 termed as S2240 are used in this thesis.

1.2 Advantages and Disadvantages of FDTD

As seen from equations above, conventional FDTD is a method which utilizes difference equations that are second-order in space and second-order in time. It provides simple, intuitive and explicit solution to Maxwell's Equations. The equations represent simple addition, subtraction and multiplication computations. Since this is a time domain transient simulation, it represents the real-time fields and is easy to parallelize.

The conventional FDTD, based on second-order central difference formula, is useful only so long as the electrical size of the structure is small. Phase error accumulates in the field calculations as the dimensions of the numerical FDTD lattice become larger. When FDTD is used to model electrically large problems, super-fine grids are required that need to get ever denser the larger the problem gets. The result is a quickly approached computing resources ceiling that limits FDTD's applicability to moderate-sized problem at best [2]. For this reason, other higher order FDTD schemes that can control such phase errors are implemented. Next section discusses the implementation method of one such scheme, which is, the finite-volumes based finite-difference time-domain (FDTD) (FV24) algorithm.

Chapter 2

Higher Order FDTD (FV24)

The finite-volumes based finite-difference time-domain (FDTD) (FV24) algorithm [3] is a high-order FDTD method designed to counter the effect of relatively large phase errors in propagated waves when a coarse grid is used. Thus, The Finite Volumes-Based 3-D second-order in time, fourth-order in space (FV24) modeling is highly capable of controlling phase errors which conventional FDTD is not capable of. High-order FDTD variants aim, in general, to provide controlled and greatly reduced phase errors when using grid resolutions in the order of 10–20 cells per wavelength for modelling problem sizes ranging from dozens to hundreds of wavelengths. Comparisons with other high-order algorithms have demonstrated that the FV24 and its two-dimensional (2D) version, the M24 algorithm [4], exhibit the highest level of phase preservation performance [3, 5]. Another advantage to the FV24 algorithm over other high-order FDTD algorithms is the continued development it has received in the form of specially designed modelling tools that preserve the algorithm's phase performance. One such example is the convolutional perfectly-matched-layer absorbing boundary conditions [6]. In the remainder of this thesis, the standard Yee scheme (conventional FDTD) will be referred to as the S22 scheme and the Finite-volumes based FDTD scheme as the FV24 scheme.

2.1 FV24 Implementation

As discussed in previous section, the standard Yee update equation for E_x is contributed to by the side walls of the cube enclosing E_x. However, there is no contribution from the front and back cube faces relative to E_x's orientation. In FV24, an outer enclosing surface is included, which is split into three distinct enclosing surfaces. Each of these provides differently weighted

and optimized contributions to the combined update equation [3].

Therefore, along with the four tangential H nodes contributing to the E_x update equation, FV24 algorithm includes contribution from axial H nodes, surface-axial H nodes and surface-diagonal H nodes. The four tangential H nodes exist on the inner surface region and are assumed to carry a weight K_a. The four axial H nodes exist on the outer enclosing surface and carry weight K_b. The four surface-axial H nodes, with a weight K_c also exist on the outer surface. Lastly, the four surface-diagonal H nodes, present on the outer enclosing surface have a weight K_c. This is shown in Fig 2.2 [3]. Fig 2.1 shows the FDTD cubic cell, while Fig 2.2 shows the FV24 cubic cells. Thus, Fig 2.1-2.2 show the comparison between the FDTD and FV24 cubic cells for E_x update equation.

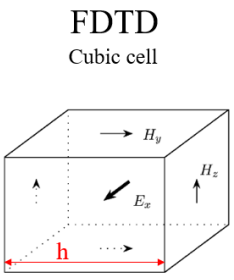

Figure 2.1: FDTD cubic cell for E_x

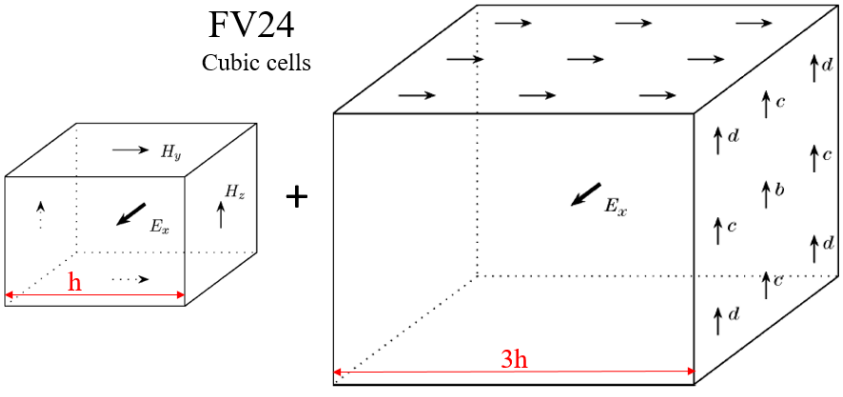

Figure 2.2: FV24 cubic cells for E_x

In Fig 2.2, 'b' represents axial H nodes, 'c' represents surface axial H nodes and 'd'

represents surface diagonal H nodes. The E_x update equations for FV24 algorithm as given by Dr. Hadi[3] are shown below:

$$\epsilon \frac{\partial E_x}{\partial t} = (K_a D_y^a + K_b D_y^b + K_c D_y^c + K_d D_y^d)\, H_z$$

$$-(K_a D_z^a + K_b D_z^b + K_c D_z^c + K_d D_z^d)\, H_y \qquad (2.1)$$

$$\epsilon \frac{\partial E_y}{\partial t} = (K_a D_z^a + K_b D_z^b + K_c D_z^c + K_d D_z^d)\, H_x$$

$$-(K_a D_x^a + K_b D_x^b + K_c D_x^c + K_d D_x^d)\, H_z \qquad (2.2)$$

$$\epsilon \frac{\partial E_z}{\partial t} = (K_a D_x^a + K_b D_x^b + K_c D_x^c + K_d D_x^d)\, H_y$$

$$-(K_a D_y^a + K_b D_y^b + K_c D_y^c + K_d D_y^d)\, H_x \qquad (2.3)$$

$$\mu \frac{\partial H_x}{\partial t} = (K_a D_z^a + K_b D_z^b + K_c D_z^c + K_d D_z^d)\, E_y$$

$$-(K_a D_y^a + K_b D_y^b + K_c D_y^c + K_d D_y^d)\, E_z \qquad (2.4)$$

$$\mu \frac{\partial H_y}{\partial t} = (K_a D_x^a + K_b D_x^b + K_c D_x^c + K_d D_x^d)\, E_z$$

$$-(K_a D_z^a + K_b D_z^b + K_c D_z^c + K_d D_z^d)\, E_x \qquad (2.5)$$

$$\mu \frac{\partial H_z}{\partial t} = (K_a D_y^a + K_b D_y^b + K_c D_y^c + K_d D_y^d)\, E_x$$

$$-(K_a D_x^a + K_b D_x^b + K_c D_x^c + K_d D_x^d)\, E_y \qquad (2.6)$$

Where

$$D_y^a H_z = \frac{1}{h}\left[H_z|_{j+\frac{1}{2}} - H_z|_{j-\frac{1}{2}}\right] \tag{2.7}$$

$$D_z^a H_y = \frac{1}{h}\left[H_y|_{k+\frac{1}{2}} - H_y|_{k-\frac{1}{2}}\right] \tag{2.8}$$

$$D_y^b H_z = \frac{1}{3h}\left[H_z|_{j+\frac{3}{2}} - H_z|_{j-\frac{3}{2}}\right] \tag{2.9}$$

$$D_y^b H_y = \frac{1}{3h}\left[H_y|_{k+\frac{3}{2}} - H_y|_{k-\frac{3}{2}}\right] \tag{2.10}$$

$$D_y^c H_z = \frac{1}{12h}\left[H_z|_{i+1,j+\frac{3}{2}} + H_z|_{i-1,j+\frac{3}{2}} + H_z|_{j+\frac{3}{2},k+1} + H_z|_{j+\frac{3}{2},k-1} - H_z|_{i+1,j-\frac{3}{2}} - H_z|_{i-1,j-\frac{3}{2}} - H_z|_{j-\frac{3}{2},k+1} - H_z|_{j-\frac{3}{2},k-1}\right] \tag{2.11}$$

$$D_z^c H_y = \frac{1}{12h}\left[H_y|_{j+1,k+\frac{3}{2}} + H_y|_{j-1,k+\frac{3}{2}} + H_y|_{i+1,k+\frac{3}{2}} + H_y|_{i-1,k+\frac{3}{2}} - H_y|_{j+1,k-\frac{3}{2}} - H_y|_{j-1,k-\frac{3}{2}} - H_y|_{i+1,k-\frac{3}{2}} - H_y|_{i-1,k-\frac{3}{2}}\right] \tag{2.12}$$

$$D_y^d H_z = \frac{1}{12h}\left[H_z|_{i+1,j+\frac{3}{2},k+1} + H_z|_{i-1,j+\frac{3}{2},k+1} + H_z|_{i+1,j+\frac{3}{2},k-1} + H_z|_{i-1,j+\frac{3}{2},k-1} - H_z|_{i+1,j-\frac{3}{2},k+1} - H_z|_{i-1,j-\frac{3}{2},k+1} - H_z|_{i+1,j-\frac{3}{2},k-1} - H_z|_{i-1,j-\frac{3}{2},k-1}\right] \tag{2.13}$$

$$D_y^d H_y = \frac{1}{12h}\left[H_y|_{i+1,j+1,k+\frac{3}{2}} + H_y|_{i-1,j+1,k+\frac{3}{2}} + H_y|_{i+1,j-1,k+\frac{3}{2}} + H_y|_{i-1,j-1,k+\frac{3}{2}} - H_y|_{i+1,j+1,k-\frac{3}{2}} - H_y|_{i-1,j+1,k-\frac{3}{2}} - H_y|_{i+1,j-1,k-\frac{3}{2}} - H_y|_{i-1,j-1,k-\frac{3}{2}}\right] \tag{2.14}$$

In this study, a resolution of R=20 cells/wavelength is taken for FV24 computation. For R=20, parameter values are [3]:

$$K_b = -0.104042707,$$

$$K_c = -0.022923377,$$

$$K_d = 0.034956192,$$

$$K_a = 1- K_b - K_c - K_d. \qquad (2.15)$$

These values have been taken such that the global phase error is minimum. The time step dt for FV24 is:

$$dt=courant\_factor*3*h/(c_o*abs(3-4* K_b -2* K_c -4* K_d)*sqrt(3)) \qquad (2.16)$$

where courant_factor is a stability criterion which represents the Courant-Friedrichs-Lewy (CFL) condition [16] for the FDTD method. For this thesis, the following values are taken for parameters in equation 2.16.

c_o =3* e-8 m/s represents the speed of light in vacuum.

h represents the spacial distance or resolution of unit cell.

courant_factor=0.9

Chapter 3

Frequency Dispersion

In this thesis work, material dispersion of dispersive objects is modeled. In previous chapters, while developing the updating equations for 3-D FDTD (S22 and FV24), the electromagnetic material properties – permittivity, permeability, and conductivities –were treated as constants for a medium. Such material models are called as simple material models. These materials have constant Permittivity (ϵ_r) across Frequencies. The conductors in these material models are considered Perfect electric conductor (PEC). Thus, they do not have conductor loss and therefore, no skin-depth. Sine the equations are relatively simple, they do not require complex computation, thereby, making the FDTD implementation simple. The FDTD algorithms for these models are fast and easily parallelizable. These are ideal models and do not represent realistic scenarios.

In practical material models, values of material parameters vary significantly as functions of frequency in the frequency band of interest. They have frequency dependent dielectric permittivity, permeability and conductor loss. To model such materials, FDTD update equations are modified to include material dispersion, making the equations relatively complex. Therefore, these models take longer to simulate and run. Also, parallelizing these models is complex. Examples of these materials are glass weave in microstrip, biological tissues, earth and artificial metamaterials.

This work models the frequency dependence of material dielectric permittivity (ε_r) using an Auxiliary Differential Equation (ADE), a technique extensively discussed in the literature [17]. To account for material dispersion, the derivation of ADE is extended for FV24 by modifying the electric field update equations. A Multi-pole Debye model, which

provides an auxiliary differential equation in time domain and produces a causal response, is used in the current analysis. This model, suitable for FDTD simulations, can simulate relative permittivity of materials with high degree of accuracy over a wide bandwidth.

In this thesis, two different dispersive models are considered. First, the material dispersion is implemented on a simple dielectric cube. Later, the dispersion modeling is performed on a more complex model, which is, breast tumor model. To model this breast tumor, two concentric dispersive spheres with different material properties are considered. The outer sphere is assumed to be the tissue, while the inner sphere is assumed as the tumor. This model represents realistic scenario and therefore, can have biological applications. Multi-pole Debye model is employed on both models.

In this chapter, the FDTD implementation of multi-pole Debye model is explained for both conventional FDTD and FV24.

3.1 Multi-Pole Debye Model

Multi-pole Debye model is suitable for modeling frequency variation of dielectric permittivity in FDTD simulations. It provides close fit over wide bandwidth. In multi-pole Debye model, the dielectric permittivity of a dispersive medium with P poles is expressed as shown in equation 3.1 [17].

$$\epsilon_r = \epsilon_\infty + \sum_{k=1}^{8} \frac{A_k(\epsilon_s - \epsilon_\infty)}{1 + j\omega\tau_k} + \frac{\sigma_{DC}}{j\omega\epsilon_0} \qquad (3.1)$$

Where ϵ_r is the relative permittivity of the medium at frequency of interest. ϵ_∞ is the relative permittivity of the medium at infinite frequencies, ϵ_s is the static relative permittivity, A_k is the amplitude of the kth term, and and τ_k is the relaxation time of the kth term. ϵ_0 is the dielectric permittivity of free space. ω is the angular frequency in rad/s and σ_{DC} is the static conductivity or conductivity at 0 frequency (DC).

In the frequency domain, the kth polarization current $\bar{J}_k$ can be written for Debye model

as

$$\bar{J}_k = j\omega\epsilon_0 \frac{A_k(\epsilon_s - \epsilon_\infty)}{1 + j\omega\tau_k} \bar{E} = \frac{j\omega\zeta_k}{1 + j\omega\tau_k} \bar{E} \tag{3.2}$$

Here $\zeta_k = A_k(\epsilon_s - \epsilon_\infty)$. For P poles, the total polarization current is written as shown in equation 3.3.

$$\sum_{k=1}^{P} \bar{J}_k = j\omega\epsilon_0 \sum_{k=1}^{P} \frac{A_k(\epsilon_s - \epsilon_\infty)}{1 + j\omega\tau_k} \bar{E} \tag{3.3}$$

Equation 3.2 can be re-arranged as shown in equation 3.4.

$$j\omega\tau_k \tilde{J}_k = j\omega\zeta_k \tilde{E} \tag{3.4}$$

Since FDTD is a time domain algorithm, the polarization current of 3.4 in frequency domain needs to be transformed to time domain. This is done using Auxiliary Differential Equation (ADE) as shown in equation 3.5.

$$\bar{J}_k + \tau_k \frac{\partial \bar{J}_k}{\partial t} = \zeta_k \frac{\partial \bar{E}}{\partial t} \tag{3.5}$$

Maxwell's Ampere's law in time domain is updated to include the polarization current as shown in equation 3.6.

$$\nabla X \bar{H} = \varepsilon_0 \varepsilon_\infty \frac{\partial \bar{E}}{\partial t} + \sigma \bar{E} + \Sigma_{k=1}^{P} \bar{J}_k \tag{3.6}$$

However, Maxwell's Faraday's Law remains unchanged as shown below.

$$\nabla X \bar{E} = -\mu \frac{\partial \bar{H}}{\partial t} \tag{3.7}$$

This implies, the magnetic field update equation is the usual equation for all components as shown below.

$\bar{H}^{n+0.5}$= Usual Magnetic Field Update Equation (3.8)

However, the electric field update equation is modified as shown in equation 3.9. The circled terms are the additional terms added to the usual electric field update equation.

$$\bar{E}^{n+1} = \frac{2\Delta t}{(2\varepsilon_0\varepsilon_\infty+\sigma\Delta t+\xi)} \nabla X \bar{H}^{n+0.5} - \frac{2\varepsilon_0\varepsilon_\infty-\sigma\Delta t+\xi}{(2\varepsilon_0\varepsilon_\infty+\sigma\Delta t+\xi)} \bar{E}^{n} - \frac{2\Delta t}{(2\varepsilon_0\varepsilon_\infty+\sigma\Delta t+\xi)} \sum_{k=1}^{P} \frac{2\tau_k}{(2\tau_k+\Delta t)} \bar{J}_k \qquad (3.9)$$

Where $\xi = \sum_{k=1}^{P} \frac{2\Delta t\zeta_k}{(2\tau_k+\Delta t)}$

The auxiliary update equation is shown in equation 3.10:

$$\bar{J}_k^{n+1} = \frac{(2\tau_k-\Delta t)}{(2\tau_k+\Delta t)} \bar{J}_k^{n} + \frac{2\zeta_k}{2\tau_k+\Delta t} (\bar{E}^{n+1} - \bar{E}^{n}) \qquad (3.10)$$

As can be seen, the multi-pole Debye equations are differential only with respect to time and not space.

The algorithm to compute the field components and polarization current is explained here as shown in fig 3.1 [17].

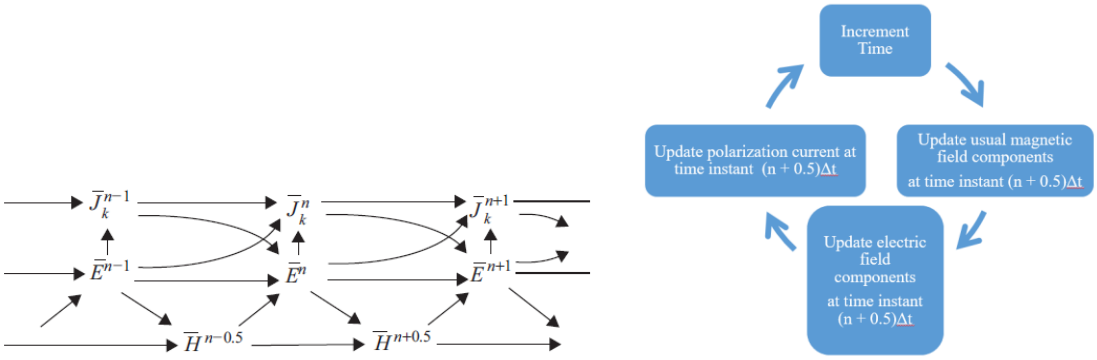

Figure 3.1: Update sequence of fields in the Debye modeling algorithm

At every time step, magnetic field components are updated as usual. Next, electric field components are updated using the past values of electric and magnetic

field components, as well as the polarization current components following equation 3.9. Then, the polarization components are calculated using the current and past values of electric field components and the past values of the polarization current components following equation 3.10. This formulation requires an additional array to store to implement equation 3.10.

Next sections discuss the update equations and coefficients for S22 and FV24.

3.2 Dispersive Equations for S22

From previous section, the update equations for electric field for S22 can be modified to include the dispersive terms. In chapter 1, the update equations for electric field without dispersion were derived. The coefficients for each term would be modified in this section to include the dispersion.

The coefficients for each term in update equation for $E_x^{n+1}(i,j,k)$ which was previously shown in equation 1.18 is modified as shown in equation 3.11.

$$C_{exe}(i,j,k) = \frac{2\varepsilon_0\varepsilon_x(i,j,k) - \Delta t\sigma_x^e(i,j,k) + \xi}{2\varepsilon_0\varepsilon_x(i,j,k) + \Delta t\sigma_x^e(i,j,k) + \xi}$$

$$C_{exhz}(i,j,k) = \frac{2\Delta t}{(2\varepsilon_0\varepsilon_x(i,j,k) + \Delta t\sigma_x^e(i,j,k) + \xi)\Delta y}$$

$$C_{exhy}(i,j,k) = -\frac{2\Delta t}{(2\varepsilon_0\varepsilon_x(i,j,k) + \Delta t\sigma_x^e(i,j,k) + \xi)\Delta z} \qquad (3.11)$$

So, the $E_x^{n+1}(i,j,k)$ update equation is as shown below:

$$E_x^{n+1}(i,j,k) = C_{exe}(i,j,k)X\ E_x^n(i,j,k)$$
$$+C_{exhz}(i,j,k)\text{X}\ (H_z^{n+\frac{1}{2}}(i,j,k) - H_z^{n+\frac{1}{2}}(i,j-1,k))$$
$$+C_{exhy}(i,j,k)\text{X}\ (H_y^{n+\frac{1}{2}}(i,j,k) - H_y^{n+\frac{1}{2}}(i,j,k-1))$$

$$- \frac{2\Delta t}{(2\varepsilon_0\varepsilon_x+\sigma_x^e(i,j,k)\Delta t+\xi)}\sum_{k=1}^{P}\frac{2\tau_k}{(2\tau_k+\Delta t)}\bar{J}_{xk} \qquad (3.12)$$

The ADE for polarization current $\bar{J}_k^{\,n+1}$ is shown in equation 3.13

$$\bar{J}_{xk}^{n+1} = \frac{(2\tau_k-\Delta t)}{(2\tau_k+\Delta t)}\bar{J}_{xk}^{n} + \frac{2\zeta_k}{2\tau_k+\Delta t}(\bar{E}_x^{n+1} - \bar{E}_x^{n}) \qquad (3.13)$$

Similarly, the coefficients for each term in update equation for $E_y^{n+1}(i,j,k)$ which was previously shown in equation 1.20 is modified as shown in equation 3.14.

$$C_{eye}(i,j,k) = \frac{2\varepsilon_0\varepsilon_y(i,j,k) - \Delta t\sigma_y^e(i,j,k) + \xi}{2\varepsilon_0\varepsilon_y(i,j,k) + \Delta t\sigma_y^e(i,j,k) + \xi}$$

$$C_{eyhx}(i,j,k) = \frac{2\Delta t}{\left(2\varepsilon_0\varepsilon_y(i,j,k) + \Delta t\sigma_y^e(i,j,k) + \xi\right)\Delta z}$$

$$C_{eyhz}(i,j,k) = -\frac{2\Delta t}{\left(2\varepsilon_0\varepsilon_y(i,j,k)+\Delta t\sigma_y^e(i,j,k)+\xi\right)\Delta x} \qquad (3.14)$$

So, the $E_y^{n+1}(i,j,k)$ update equation is as shown below:

$$E_y^{n+1}(i,j,k) = C_{eye}(i,j,k)X\ E_y^{n}(i,j,k)$$

$$+C_{eyhx}(i,j,k)\text{X}(\ H_x^{n+\frac{1}{2}}(i,j,k) - H_x^{n+\frac{1}{2}}(i,j,k-1))$$

$$+C_{eyhz}(i,j,k)\text{X}\ (H_z^{n+\frac{1}{2}}(i,j,k) - H_z^{n+\frac{1}{2}}(i-1,j,k))$$

$$- \frac{2\Delta t}{(2\varepsilon_0\varepsilon_x+\sigma_y^e(i,j,k)\Delta t+\xi)}\Sigma_{k=1}^{P}\frac{2\tau_k}{(2\tau_k+\Delta t)}\bar{J}_{yk} \qquad (3.15)$$

The ADE for polarization current is shown in equation 3.16

$$\bar{J}_{yk}^{n+1} = \frac{(2\tau_k-\Delta t)}{(2\tau_k+\Delta t)}\bar{J}_{yk}^{n} + \frac{2\zeta_k}{2\tau_k+\Delta t}(\bar{E}_y^{n+1} - \bar{E}_y^{n}) \qquad (3.16)$$

Similarly, the coefficients for each term in update equation for $E_y^{n+1}(i,j,k)$ which was previously shown in equation 1.22 is modified as shown in equation 3.17.

$$C_{eze}(i,j,k) = \frac{2\varepsilon_0\varepsilon_z(i,j,k) - \Delta t\sigma_z^e(i,j,k) + \xi}{2\varepsilon_0\varepsilon_z(i,j,k) + \Delta t\sigma_z^e(i,j,k) + \xi}$$

$$C_{ezhy}(i,j,k) = \frac{2\Delta t}{(2\varepsilon_0\varepsilon_z(i,j,k) + \Delta t\sigma_z^e(i,j,k) + \xi)\Delta x}$$

$$C_{ezhx}(i,j,k) = -\frac{2\Delta t}{(2\varepsilon_0\varepsilon_z(i,j,k)+\Delta t\sigma_z^e(i,j,k)+\xi)\Delta y} \qquad (3.17)$$

So, the $E_z^{n+1}(i,j,k)$ update equation is as shown below:

$$E_z^{n+1}(i,j,k) = C_{eze}(i,j,k)X\ E_z^n(i,j,k)$$
$$+C_{ezhy}(i,j,k)\text{X}\ (H_y^{n+\frac{1}{2}}(i,j,k) - H_y^{n+\frac{1}{2}}(i-1,j,k))$$
$$+C_{ezhx}(i,j,k)\text{X}\ (H_x^{n+\frac{1}{2}}(i,j,k) - H_x^{n+\frac{1}{2}}(i,j-1,k))$$
$$-\frac{2\Delta t}{(2\varepsilon_0\varepsilon_z+\sigma_z^e(i,j,k)\Delta t+\xi)}\sum_{k=1}^{P}\frac{2\tau_k}{(2\tau_k+\Delta t)}\bar{J}_{zk} \qquad (3.18)$$

The ADE for polarization current is shown in equation 3.19

$$\bar{J}_{zk}^{n+1} = \frac{(2\tau_k-\Delta t)}{(2\tau_k+\Delta t)}\bar{J}_{zk}^n + \frac{2\zeta_k}{2\tau_k+\Delta t}(\bar{E}_z^{n+1} - \bar{E}_z^n) \qquad (3.19)$$

3.3 Dispersive Equations for FV24

From section 3.1, the update equations for electric field for FV2420 can be modified to include the dispersive terms. In chapter 2, the update equations for electric field without dispersion were derived. The coefficients for each term would be modified in this section to include the dispersion.

The below equation shows the coefficients of $E_x^{n+1}(i,j,k)$ modified to include dispersive terms:

$$C_{ax}(i,j,k) = \frac{2\varepsilon_0\varepsilon_x(i,j,k) - \Delta t\sigma_x^e(i,j,k) + \xi}{2\varepsilon_0\varepsilon_x(i,j,k) + \Delta t\sigma_x^e(i,j,k) + \xi}$$

$$C_{b1x}(i,j,k) = k4a * \frac{2\Delta t}{(2\varepsilon_0\varepsilon_x(i,j,k) + \Delta t\sigma_x^e(i,j,k) + \xi)\Delta y}$$

$$C_{b2x}(i,j,k) = k1a * \frac{2\Delta t}{(2\varepsilon_0\varepsilon_x(i,j,k) + \Delta t\sigma_x^e(i,j,k) + \xi)\Delta y}$$

$$C_{b3x}(i,j,k) = k2a * \frac{2\Delta t}{(2\varepsilon_0\varepsilon_x(i,j,k) + \Delta t\sigma_x^e(i,j,k) + \xi)\Delta y}$$

$$C_{b4x}(i,j,k) = k3a * \frac{2\Delta t}{(2\varepsilon_0\varepsilon_x(i,j,k) + \Delta t\sigma_x^e(i,j,k) + \xi)\Delta y} \quad (3.20)$$

For R=20, the following values given in Table 3.1 are used to reduce phase error as shown in Chapter 2. Here, k1a=k1/3; k2a=k2/12; k3a=k3/12; k4a=k4;

Table 3.1: FV2420 parameter values

Parameter	Value
k1	-0.104042707
k2	-0.022923377
k3	0.034956192
k4	1-k1-k2-k3

The electric field update equation $E_x^{n+1}(i,j,k)$ is as shown below:

$$E_x^{n+1}(i,j,k) = C_{ax}(i,j,k)E_x^n(i,j,k)$$

$$+C_{b1x}(i,j,k)\left(\left[H_z|_{j+\frac{1}{2}} - H_z|_{j-\frac{1}{2}}\right] - \left[H_y|_{k+\frac{1}{2}} - H_y|_{k-\frac{1}{2}}\right]\right)$$

$$+C_{b2x}(i,j,k)\left(\left[H_z|_{j+\frac{3}{2}}-H_z|_{j-\frac{3}{2}}\right]-\left[H_y|_{k+\frac{3}{2}}-H_y|_{k-\frac{3}{2}}\right]\right)$$

$$+C_{b3x}(i,j,k)\left(\left[H_z|_{i+1,j+\frac{3}{2}}+H_z|_{i-1,j+\frac{3}{2}}+H_z|_{j+\frac{3}{2},k+1}+H_z|_{j+\frac{3}{2},k-1}-H_z|_{i+1,j-\frac{3}{2}}-H_z|_{i-1,j-\frac{3}{2}}-H_z|_{j-\frac{3}{2},k+1}-H_z|_{j-\frac{3}{2},k-1}\right]-\left[H_y|_{j+1,k+\frac{3}{2}}+H_y|_{j-1,k+\frac{3}{2}}+H_y|_{i+1,k+\frac{3}{2}}+H_y|_{i-1,k+\frac{3}{2}}-H_y|_{j+1,k-\frac{3}{2}}-H_y|_{j-1,k-\frac{3}{2}}-H_y|_{i+1,k-\frac{3}{2}}-H_y|_{i-1,k-\frac{3}{2}}\right]\right)$$

$$+C_{b4x}(i,j,k)\left(\left[H_z|_{i+1,j+\frac{3}{2},k+1}+H_z|_{i-1,j+\frac{3}{2},k+1}+H_z|_{i+1,j+\frac{3}{2},k-1}+H_z|_{i-1,j+\frac{3}{2},k-1}-H_z|_{i+1,j-\frac{3}{2},k+1}-H_z|_{i-1,j-\frac{3}{2},k+1}-H_z|_{i+1,j-\frac{3}{2},k-1}-H_z|_{i-1,j-\frac{3}{2},k-1}\right]-\left[H_y|_{i+1,j+1,k+\frac{3}{2}}+H_y|_{i-1,j+1,k+\frac{3}{2}}+H_y|_{i+1,j-1,k+\frac{3}{2}}+H_y|_{i-1,j-1,k+\frac{3}{2}}-H_y|_{i+1,j+1,k-\frac{3}{2}}-H_y|_{i-1,j+1,k-\frac{3}{2}}-H_y|_{i+1,j-1,k-\frac{3}{2}}-H_y|_{i-1,j-1,k-\frac{3}{2}}\right]\right)$$

$$-\frac{2\Delta t}{(2\varepsilon_0\varepsilon_x+\sigma_x^e(i,j,k)\Delta t+\xi)}\sum_{k=1}^{P}\frac{2\tau_k}{(2\tau_k+\Delta t)}\bar{J}_{xk} \qquad (3.21)$$

The ADE for polarization current $\bar{J}_{xk}^{n+1}$ is shown in equation 3.22

$$\bar{J}_{xk}^{n+1}=\frac{(2\tau_k-\Delta t)}{(2\tau_k+\Delta t)}\bar{J}_{xk}^{n}+\frac{2\zeta_k}{2\tau_k+\Delta t}(\bar{E}_x^{n+1}-\bar{E}_x^{n}) \qquad (3.22)$$

Similar equations are derived for $E_y^{n+1}(i,j,k)$ and $E_z^{n+1}(i,j,k)$ and the polarization currents $\bar{J}_{yk}^{n+1}$ and $\bar{J}_{zk}^{n+1}$. The magnetic field update equations remain unchanged.

Chapter 4

Modeling and Simulation Setup

In this thesis, the problem space considered are a simple dielectric cube and breast tumor. The dispersive parameters are different for the two models. The modeling is done in Mathworks Matlab tool. For analysis, Radar cross-section (RCS) computed by far-fields are compared between S2220, S2240 and FV2420. Moreover, these results are also compared with Ansys High Frequency Structure Simulator- Integral Equation (HFSS-IE) Solver which is a Method of Moments (MoM) software. Hence, this tool provides accurate results for comparison.

This chapter describes the simulation setup for both Matlab and HFSS-IE tool. Section 4.1 elaborates on the excitation/source for the model in this work.

4.1 Plane Wave Sources

The implementation of plane wave incidence for the model is implemented using the total-field/scattered-field (TFSF) formulation for a three-dimensional finite volumes-based, extended-stencil finite-difference time-domain (FV24) algorithm [8]. This is a leakage free technique.

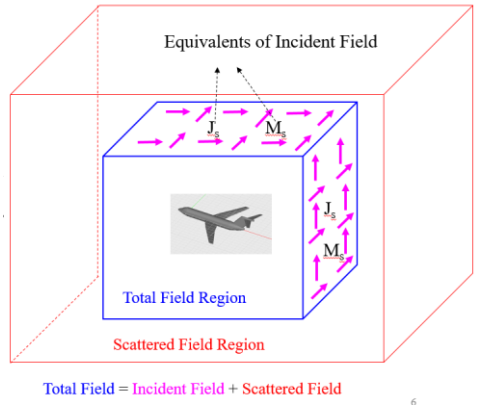

Figure 4.1: TF/SF implementation

In a TFSF implementation, the plane wave incident field is introduced strictly within the total-field region by manipulating the jump conditions at this region's enclosing surfaces. The net result is a scattered-field region that sees only the scattered fields which should be virtually zero if the scatterer is removed [8].

In this method, two regions are considered, namely, total field (TF) and scattered field (SF). A plane wave is incident at an angle which excites fields inside the total field region. Incident fields are obtained using auxiliary 1-D grid using Tan and Potter approach [9]. Using this approach, equivalent surface currents for incident electric field, J_s and equivalent surface currents for incident magnetic field, M_s are obtained. These surface currents can be written as:

$$J_s = \hat{\eta}\, X\, H_s$$

$$M_s = \hat{\eta}\, X\, E_s \tag{4.1}$$

In the above equations, E_s and H_s are the equivalent surface electric and magnetic fields respectively for equivalent electric and magnetic surface currents. Due to the staggered-in-space placement of electric and magnetic fields in FDTD Yee cell, selection of an equivalent surface harboring both tangential electric and magnetic fields is not feasible. Therefore, a closed surface with tangential electric (or magnetic) fields is selected and the neighboring magnetic (or electric) fields are interpolated using Martin-Mixed approach [10]. This brings approximate magnetic (or electric) fields on the equivalent surface. The surface currents are converted to corresponding electric and magnetic vector potentials using standard surface integral formulation. The vector potentials are calculated for an equivalent surface as shown in Fig 4.2 [1,2,11]. The surface integral equations for vector potentials are shown in equation 4.2.

$$A(\hat{r},\omega) = \frac{\mu_0 e^{-jkR}}{4\pi R} \oiint_S J_s(\hat{r},\omega) e^{jk\hat{r}.\acute{r}} dS' = \frac{\mu_0 e^{-jkR}}{4\pi R} N$$

$$F(\hat{r},\omega) = \frac{\epsilon_0 e^{-jkR}}{4\pi R} \oiint_S M_s(\hat{r},\omega) e^{jk\hat{r}.\acute{r}} dS' = \frac{\epsilon_0 e^{-jkR}}{4\pi R} L \tag{4.2}$$

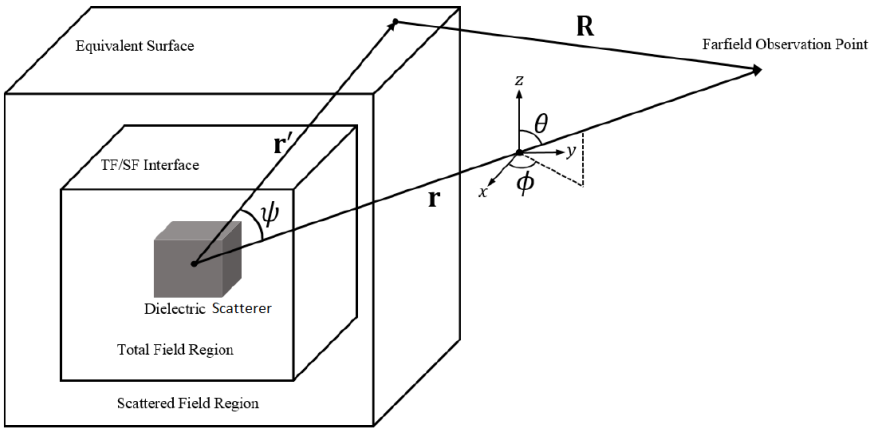

Figure 4.2: Equivalent Surface and far-field observation point

Using these potentials, far-field electric and magnetic fields at a far-field observation point are computed as shown in equation 4.3. E_θ is the electric field an elevation angle θ, H_θ is the magnetic field an elevation angle θ, E_ϕ is the electric field an azimuth angle ϕ, H_ϕ is the magnetic field an azimuth angle ϕ. This is called the near to far-field (NTFF) transformation.

$$E_\theta = -j\omega\left(A_\theta + \eta F_\varphi\right), \qquad E_\theta = -j\omega\left(A_\varphi + \eta F_\theta\right)$$

$$H_\theta = +\frac{j\omega}{\eta}\left(A_\varphi - \eta F_\theta\right),\ H_\varphi = -\frac{j\omega}{\eta}\left(A_\theta + \eta F_\varphi\right) \tag{4.3}$$

The auxiliary vectors N and L in equation 4.2, that represent only the surface integrals, and field equations 4.3 are then used to calculate the θ and ϕ components of RCS, given by equations 4.4 [1, 2, 11,18,19,20,21].

$$RCS_\theta(\theta, \emptyset, \omega) = \frac{k^2}{8\pi\eta_0 P_{inc}}|L_\emptyset + \eta_0 N_\theta|^2$$

$$RCS_\emptyset(\theta, \emptyset, \omega) = \frac{k^2}{8\pi\eta_0 P_{inc}}|L_\theta - \eta_0 N_\emptyset|^2 \tag{4.4}$$

where k and η_o are the free-space wave-number and the intrinsic impedance, respectively. P_{inc} is the power density of the incident planewave, given by

$$P_{inc} = \frac{1}{2\eta}\left(E_{\theta}^{2} + E_{\emptyset}^{2}\right) * |F(\omega)|^{2} \quad (4.5)$$

F(ω) is the Fourier transform of time-series f(t) [1,2,11,18,19,20,21]. The θ and ϕ components of the auxiliary vectors N and L are defined by equations as given in [1,2,11,18,19,20,21].

The RCS of both dielectric sphere and breast tumor are calculated using the above approach. Both models are illuminated with a plane wave at θ_{inc} = 38.0° and ϕ_{inc} = 35.5°, rendered by the choice of integers (m_x,m_y,m_z) as (7,5,11) in the perfect TF/SF formulation. These angles in FDTD indicate the direction of planewave propagation (direction of propagation vector). Contrary to this, HFSS model requires that the direction the planewave comes from (opposite to the direction of propagation vector). Consequently, the planewave arrival angles, $\theta_{arrival}$ = 180- θ_{inc} and $\phi_{arrival}$ =180 + ϕ_{inc} are used in the HFSS-IE solver. The time-profile of the theta-polarized planewave is a modulated Gaussian pulse, with frequency spectrum centered around the frequency of interest for the two models (specified later in this chapter). The no. of time-steps in FDTD is chosen such that, the electric fields in the problem space die down to 10^{-7} V/m levels.

4.2 Absorbing Boundary Conditions

Because computational storage space is finite, the finite-difference time-domain (FDTD) problem space size is finite and needs to be truncated by special boundary conditions. The types of special boundary conditions that simulate electromagnetic waves propagating continuously beyond the computational space are called absorbing boundary conditions (ABCs). However, the imperfect truncation of the problem space will create numerical reflections, which will corrupt the computational results in the problem space after certain amounts of simulation time.

In this work, Convolutional Perfectly Matched Layer (CPML) boundary conditions are used which are highly efficient at absorbing evanescent waves and signals with a long-time signature. Therefore, using the CPML, the boundaries can be placed closer to the objects in the problem space and a time and memory saving can be achieved. The CPML boundary has a

CPML depth. In this thesis, a depth of 10 cells is used on each side. The outer boundary of the CPML is a Perfect Electric Conductor (PEC). The implementation of CPML for S22 and FV24 is given in [1,6, 22].

4.3 Dielectric Cube Model

The RCS of a dielectric cube which is the dielectric scatterer ($\varepsilon_r = 4$; $\mu_r = 1$) is calculated at a single frequency of 1 GHz. A dielectric cube of size $\lambda/2$ on each side (at 1 GHz) is taken. The dielectric cube is of dispersive material with parameters as given in Table 4.1. The Matlab model for the cube is shown in Fig 4.3. The HFSS model is shown in Fig 4.4. For S2220 and FV2420, the no of time-steps taken is 2400. For S2240, the no. of time-steps is 4800. The material parameters are taken for Glass-Weave microstrip with substrate of material FR4. This material is chosen to emulate realistic dielectric scatterer. These parameters are for the Multi-pole Debye model corresponding to equations 3.1 and 3.2. The model has 8 poles. For S2220, S2240 and FV2420, the RCS is calculated at each plane and compared with the RCS computed from HFSS-IE solver.

Table 4.1: Dispersive parameters for dielectric cube

Material Parameter	Value
ϵ_∞	4
P	8
ε_s	4.0961
σ^e	0 Sm^{-1}
σ^m	0 Sm^{-1}
μ_r	1
A_k for k=1 to P	[-0.0087, 0.0282, 0.1629, 0.1504, 0.1644, 0.1503, 0.1642, 0.1560]

ω_k for k=1 to P	2*(10^3*10.^(1:8)) rad/s
τ_k for k=1 to P	1./(2*(10^3*10.^(1:8))) sec
Frequency f	1 GHz

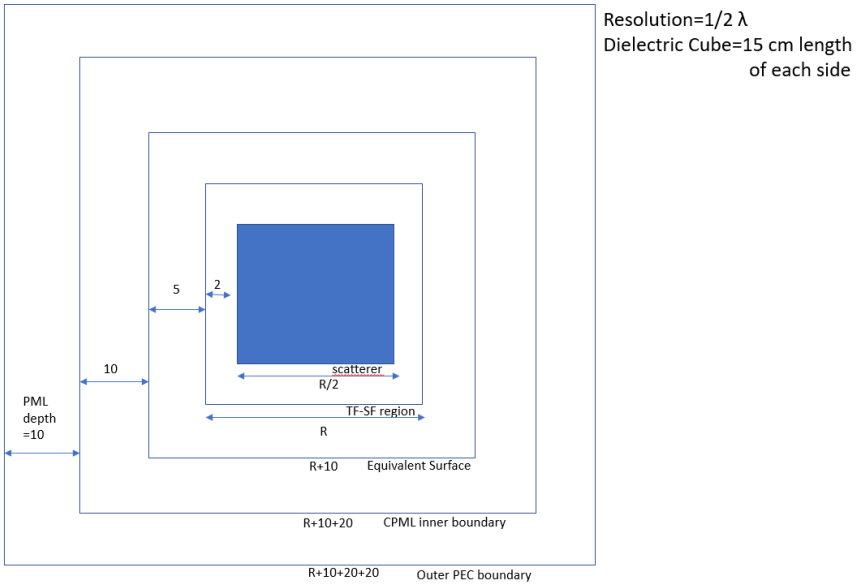

Figure 4.3: Dielectric Cube model in Matlab for λ/2 resolution

For HFSS-IE, the length of each side is 15 cm. The plane wave is incident at (x,y,z) = (0,0,0).

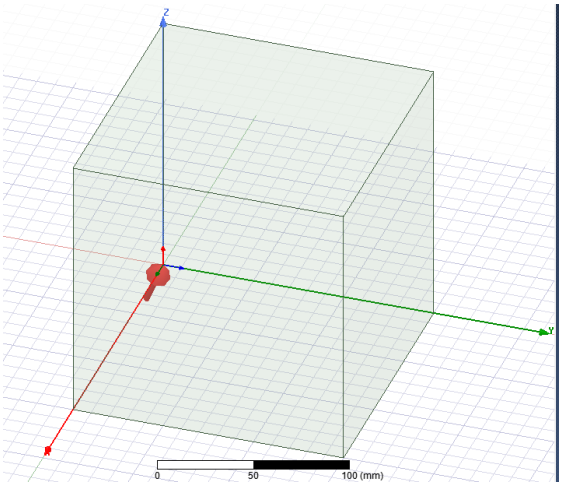

Figure 4.4: Dielectric Cube model in HFSS-IE

4.4 Breast Tumor Model

Breast tumor is modeled as two concentric spheres with different dielectric material properties. The material properties are taken from [12] which provide the Cole–Cole parameters for the dielectric properties of the breast tissue (normal samples) and tumor (cancer samples) obtained from cancer surgeries. In the Cole-Cole model given by [12], the model is a 1-pole Cole-Cole model. Cole-Cole model is a generalized equation which is good for a wide-range of fields and has applications in biology. Debye model is a special case of a Cole-Cole model.

Equation 4.6 shows the complex relative permittivity equation for 1-pole Cole-Cole model. The exponent parameter α, takes a value between 0 and 1. When α=0, the Cole-Cole model reduces to the Debye model. As can be seen, the exponential nature of the denominator in the first term in Cole-Cole equation makes it difficult to solve. The Debye model, on the other hand, is very suitable for fast computation of wideband fields. Table 4.2 shows the Cole-Cole parameters for breast tumor as given by [12]

$$\epsilon_r = \epsilon_\infty + \frac{A(\epsilon_s - \epsilon_\infty)}{(1+j\omega\tau)^{(1-\alpha)}} + \frac{\sigma_{DC}}{j\omega\epsilon_0} \tag{4.6}$$

Table 4.2: Cole-Cole parameters for breast tumor

Material Parameter	Value for breast tissue	Value for tumor
ϵ_∞	5.013	7.670
$\Delta\epsilon = (\epsilon_s - \epsilon_\infty)$	40.60	43.92
σ^{DC}	0.607 Sm^{-1}	0.748 Sm^{-1}
σ^{m}	0 Sm^{-1}	0 Sm^{-1}
μ_r	1	1
τ	10.16 ps	10.70 ps
α	0.091	0.028
Frequency f	10 GHz	10 GHz

The Cole-Cole Model is Converted to Multi-Pole Debye model with eight poles. This is done using nonlinear regression, a curve fitting feature in Matlab. 'nlinfit' command in Matlab executes the curve-fitting algorithm. Using this approach, respective A_k are found using Non-Linear Regression. Eight $1/\tau_k$ (Relaxation Frequencies) are chosen over Large Bandwidth (0.2 GHz to 30 GHz). This is because, the frequency of interest in this thesis is in the range 1-20 GHz. Fig 4.5 shows the curve-fitting for Real part of complex permittivity over the frequency range of 0.2 GHz to 30 GHz for breast tissue and tumor. Fig 4.6 shows the curve-fitting for imaginary part of complex permittivity and Fig 4.7 shows the curve-fitting for conductivity.

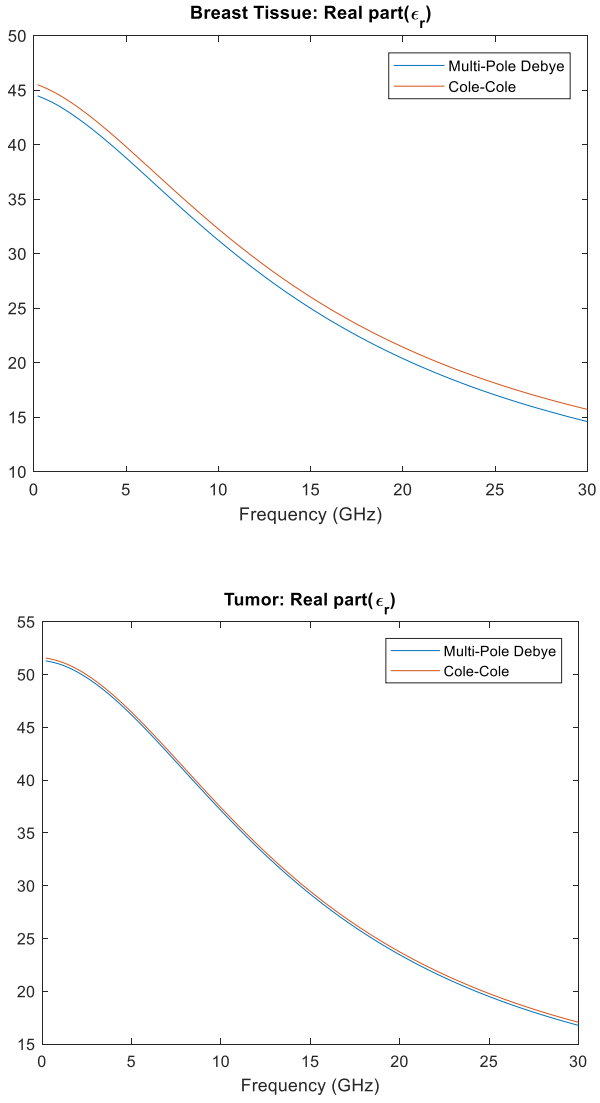

Figure 4.5: Curve-fitting for real part of complex permittivity

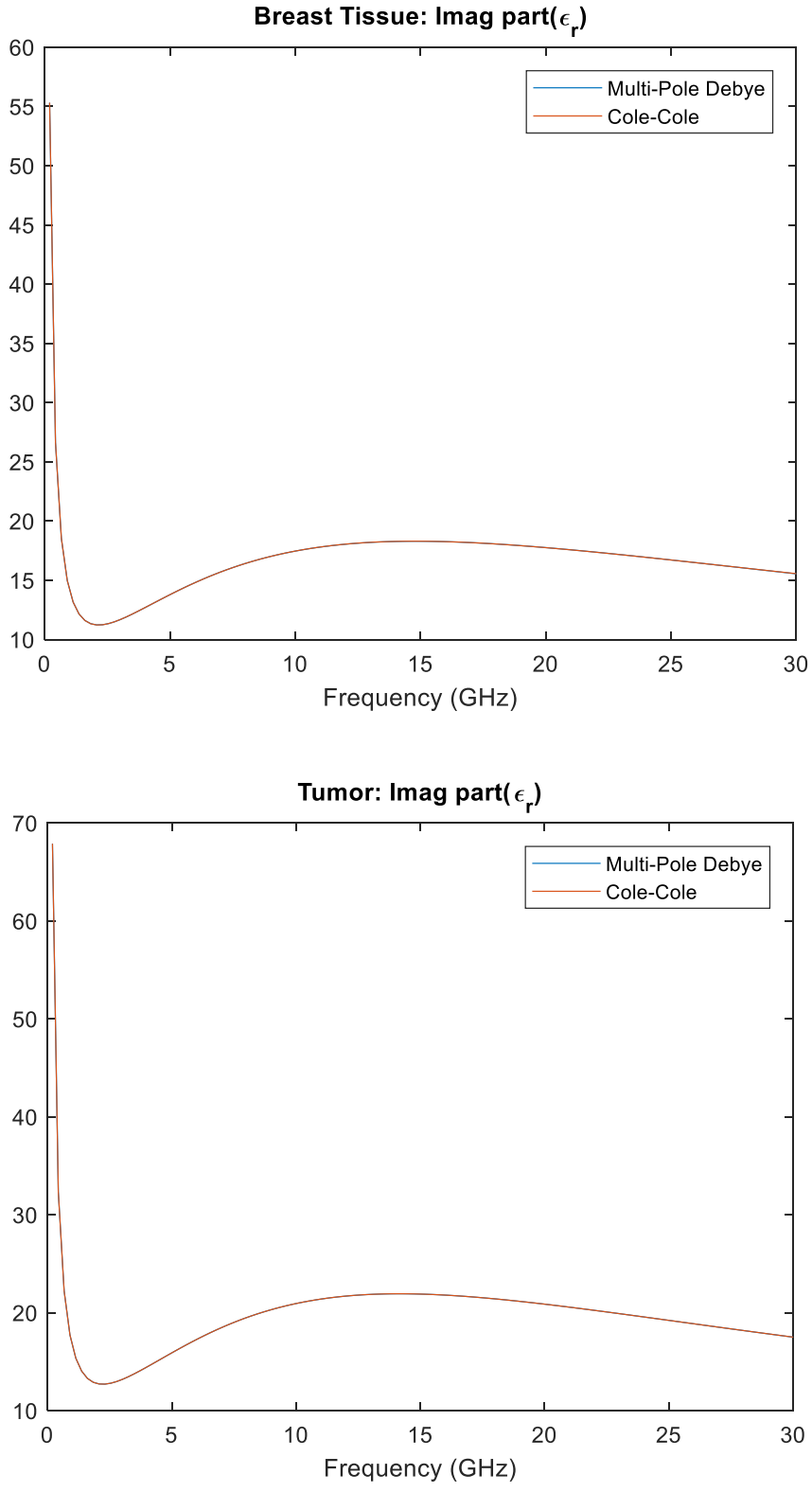

Figure 4.6: Curve-fitting for imaginary part of complex permittivity

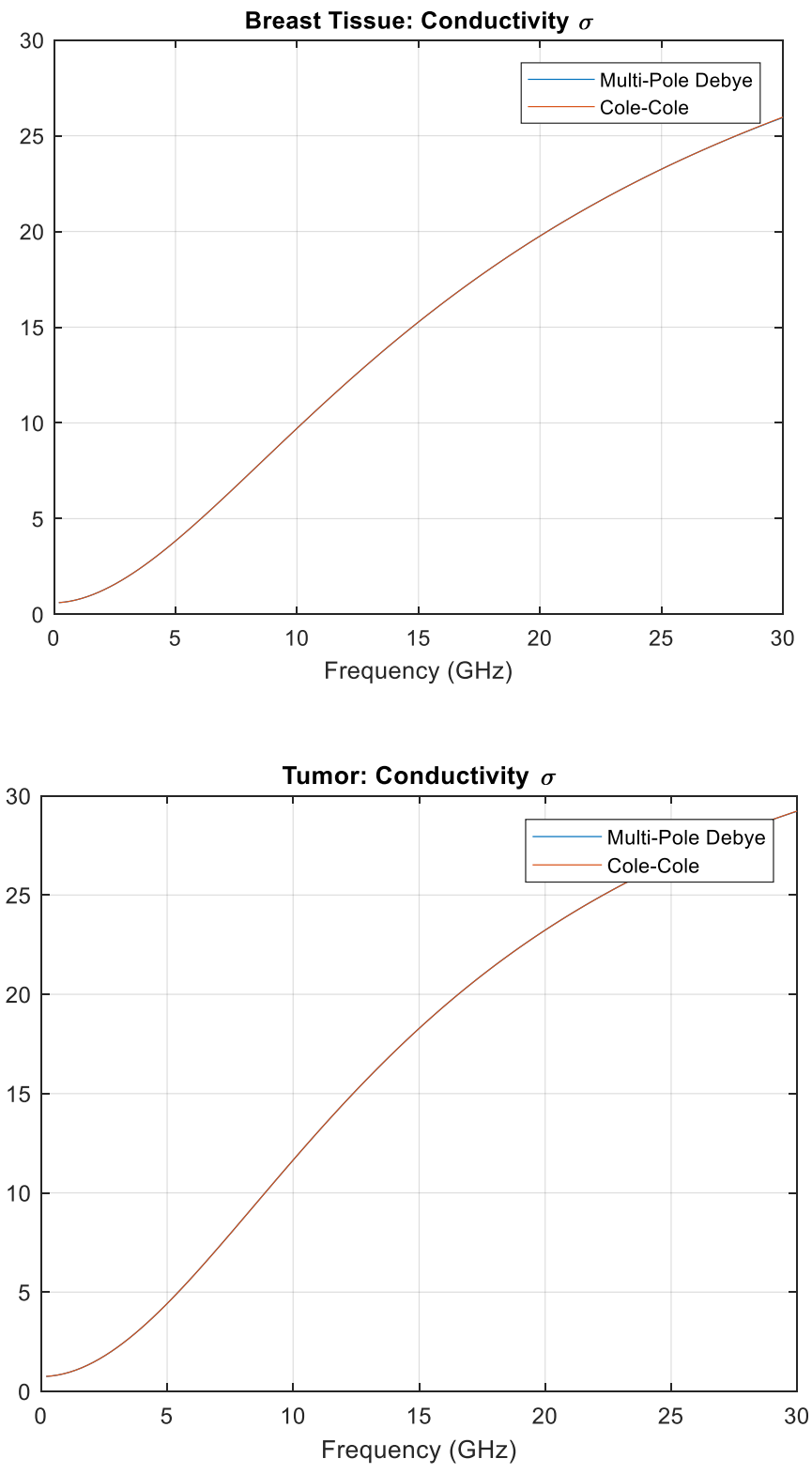

Figure 4.7: Curve-fitting for conductivity

Table 4.3 shows the multi-pole Debye parameter values for breast tissue and tumor obtained from the curve-fitting algorithm.

Table 4.3: Multi-pole dispersive parameters for Breast Tumor

Material Parameter	Breast Tissue Value	Tumor Value
ϵ_∞	5.0130	7.6700
P	8	8
ε_s	45.6130	51.5900
σ^e	0.607 Sm^{-1}	0.7480 Sm^{-1}
σ^m	0 Sm^{-1}	0 Sm^{-1}
μ_r	1	1
A_k for k=1 to P	[-0.0000, 0.0103, -0.0081, 0.0311, 0.0052, 0.1595, 0.5385, 0.2372]	[-0.0013, 0.0064, -0.0083, 0.0173, -0.0112, 0.0887, 0.8299, 0.0722]
ω_k for k=1 to P	7.363*(10^8*2.^(1:8)) rad/s	7.363*(10^8*2.^(1:8)) rad/s
τ_k for k=1 to P	1./ (7.363*(10^8*2.^(1:8))) sec	1./ (7.363*(10^8*2.^(1:8))) sec
Frequency f	10 GHz	10 GHz

The RCS results of the breast tumor model obtained from multi-pole Debye values are compared with HFSS-IE RCS results. For this model, two different structures are taken. Initially, the diameter of outer sphere is taken as λ (at 10 GHz). The diameter of inner sphere is taken as λ/2 (at 10 GHz). This corresponds to the small structure. In HFSS-IE, the diameters input into the model corresponding to these resolutions are 3 cm for outer sphere and 1.5 cm for the inner sphere. Matlab model for this small structure is shown in Fig 4.8. The unit time-step (dt) given in equations 1.29 (S22) and 2.16 (FV24) is reduced by half and the number of time steps (N) is doubled. This is done to overcome the instability in electric fields caused by higher dt and lower N. Therefore, for S2220 and FV2420, the simulation is run for 5760 time-steps.

For S2240, it is run for 10560 time-steps.

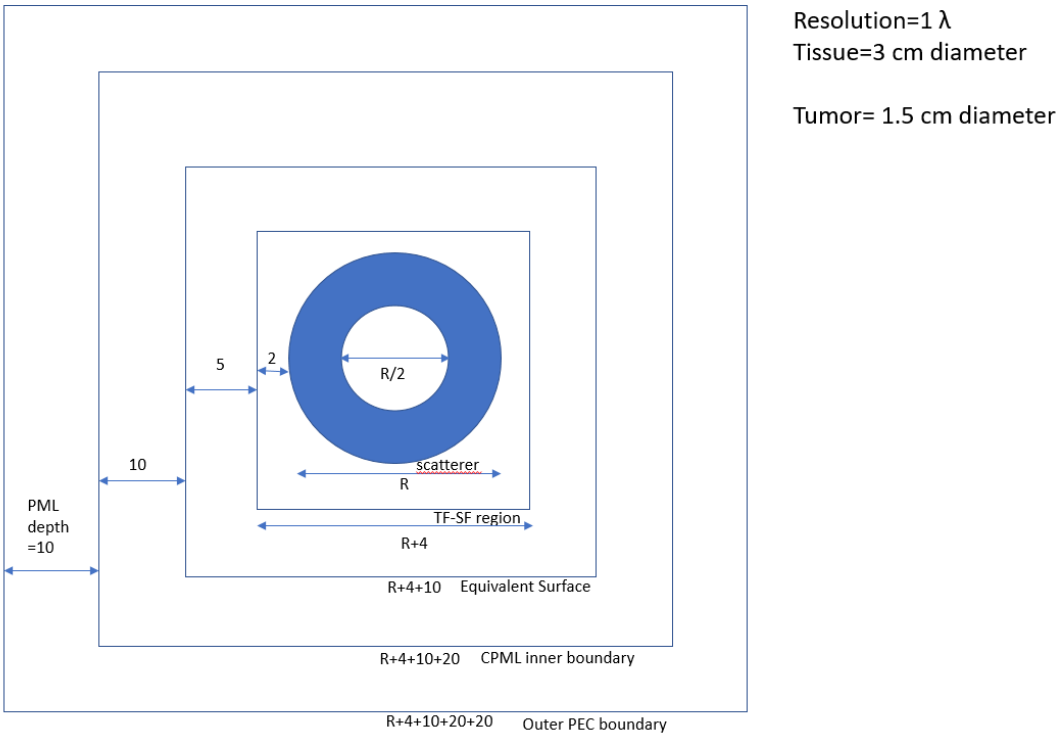

Figure 4.8: Breast tumor model in Matlab for λ resolution of outer sphere

Later, the diameter of outer sphere is taken as 4λ (at 10 GHz). The diameter of inner sphere is taken as λ (at 10 GHz). This corresponds to the electrically large structure. These dimensions are taken from [13] to emulate realistic breast tissue and tumor diameters. In HFSS-IE, the diameters input into the model corresponding to these resolutions are 12 cm for outer sphere and 3 cm for the inner sphere. Matlab model for this small structure is shown in Fig 4.9. The unit time-step (dt) given in equations 1.29 (S22) and 2.16 (FV24) is reduced by three-fourth and the number of time steps (N) is multiplied by four-third. This is done to overcome the instability in electric fields caused by higher dt and lower N. Also, this is done to reduce the simulation time (if dt is halved and N is doubled, simulation time increases). Therefore, for S2220 and FV2420, the simulation is run for 13440 time-steps. For S2240, it is run for 26240 time-steps.

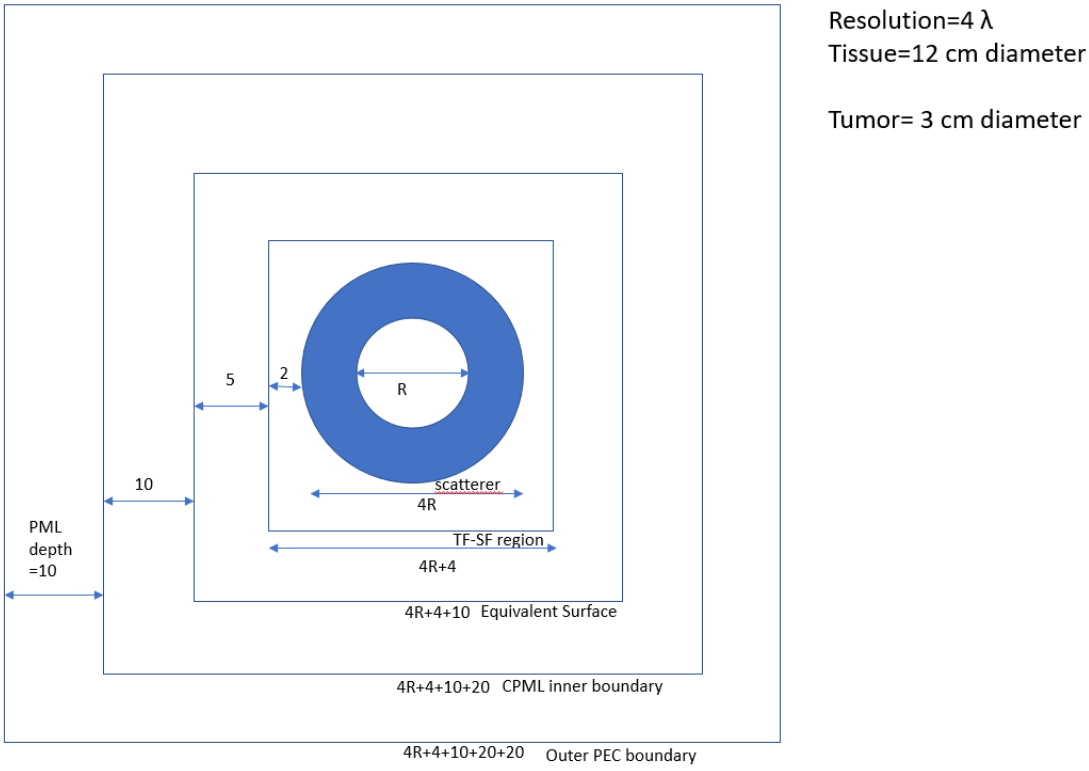

Figure 4.9: Breast tumor model in Matlab for 4λ resolution of outer sphere

Fig 4.10 shows the HFSS-IE model for the breast tumor.

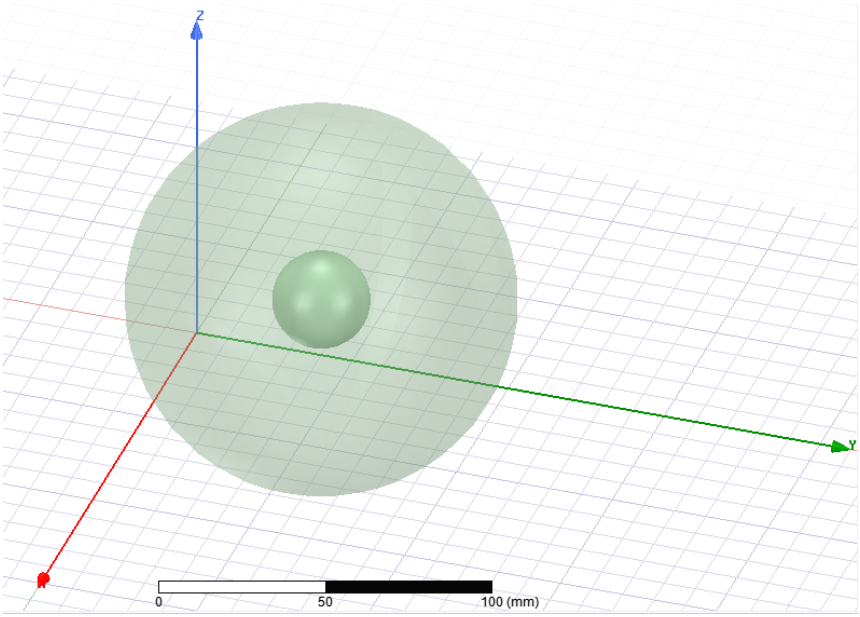

Figure 4.10: Breast tumor model in HFSS-IE

Since the FDTD grid constitutes of Yee cells, the entire problem size is made up of cubes. Hence, the material properties such as relative permittivity at the edges of the grid are taken same as that at the center of the cell. This is a reasonable approximation without loss of much accuracy. Fig 4.11 shows the relative permittivity profile in X direction (as can be seen, the profile is a staircase profile due to the cubic unit cells).

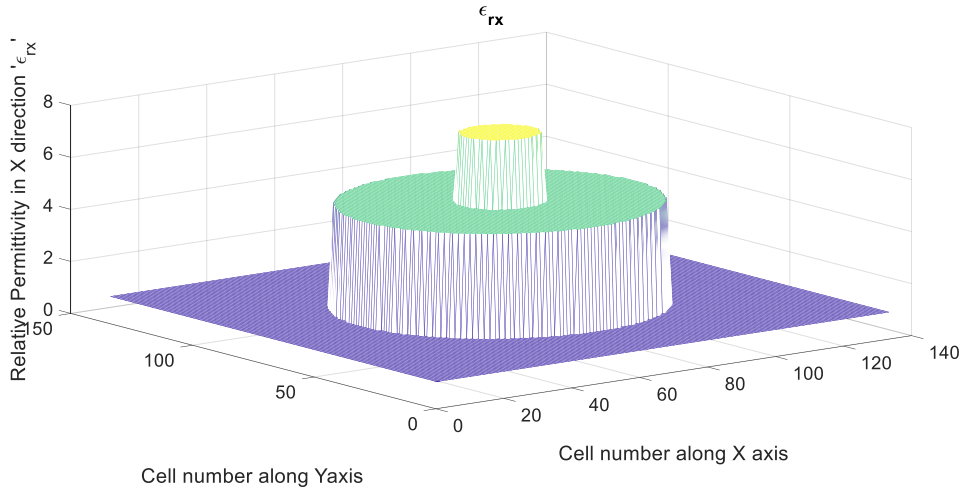

(a) Front-view

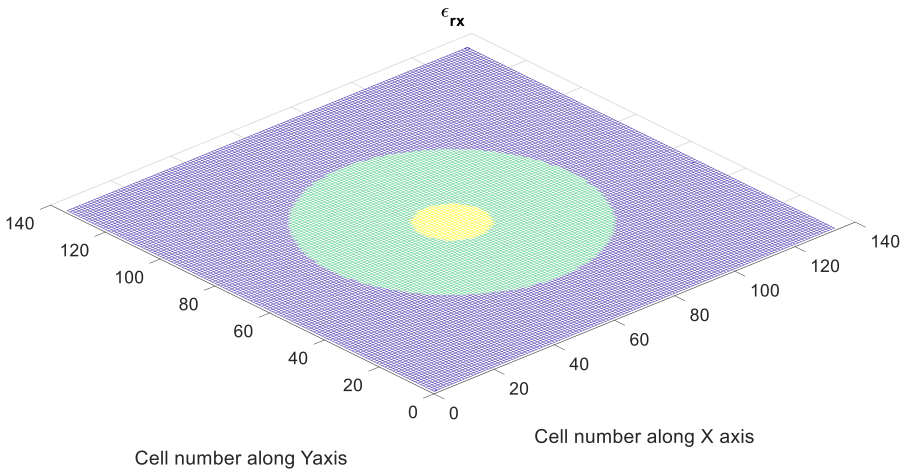

(b) Top view

Figure 4.11: X-Y cross-section for relative permittivity in X direction

4.5 Running MATLAB and HFSS-IE Models on Supercomputer

In this work, large models in MATLAB and HFSS-IE were run on Supercomputer. Research computing team at University of Colorado Boulder offers state-of-the art computing and data services. From Windows 10 desktop, login to a Research Computing resource is done to submit the job. Putty, an SSH client application is used to login to the Summit. As soon as job is submitted, it runs in the background when resources are available.

A bash script is submitted to Slurm, a batch queuing system that will schedule the job to run non-interactively when resources are available. Since all the jobs submitted are from a login node, Slurm module is loaded with the command *module load slurm/summit* before submitting any job. The script is submitted to Slurm with the command *sbatch <script_name>.sh*. The job submission script is composed of 5 parts as below [14]:

```
#!/bin/bash
#SBATCH --nodes=1                                # Number of requested nodes
#SBATCH --time=0:05:00                           # Max wall time
#SBATCH --qos=debug                              # Specify debug QOS
#SBATCH --partition=shas                         # Specify Summit haswell nodes
#SBATCH --ntasks=1                               # Number of tasks per job
#SBATCH --job-name=General-Job-Submission        # Job submission name
#SBATCH --output=GENERAL-JOB-SUBMISSION.%j.out   # Output file name with Job ID


# Written by:    Shelley Knuth
# Modified by: Daniel Trahan
# Date:              24 February 2014
# Updated:         20 April 2018
# Purpose:         This script submits a general job to the Slurm job scheduler

# purge all existing modules
module purge

# load any modules needed to run your program
module load required_module1
module load required_module2
module load required_module3

# The directory where you want the job to run
cd /projects/$USER/your_project

# Run your program
./your_program.exe
```

All the jobs submitted in this work are to Haswell nodes, which are the default nodes. On Summit, nodes with the same hardware configuration are grouped into partition, Haswell being one such partition. Table 4.4 and 4.5 list the configuration and memory information for Haswell nodes [14]. These nodes have Red Hat Enterprise Linux 7 as their Operating System.

Table 4.4: Hardware configuration for Haswell nodes

Partition name	Description	# of nodes	Cores /nodes	RAM /core (GB)	Max Wall-time	Billing weight
shas	Haswell CPUs (default)	380	24	5.25	24H	1

Table 4.5: Details on Memory for Haswell nodes

CPU	Memory	Local Storage
Intel Xeon E5-2680 v3 @2.50GHz (2 CPUs/node, 24 cores/node)	2133 MT/s, Dual Rank, x4 Data Width RDIMM, (8x16GB, 128GB/node)	200 GB SSD (1/node)

For this work, Walltime ranging upto 30 hours has been used. Summit Quality of Service (QoSes) listed in Table 4.6 have been used for the same [14]. In Summit, QoS's are used to constrain or modify the characteristics that a job can have.

Table 4.6: Summit QoS

QOS name	Description	Max walltime	Node limits	Priority boost
normal	default	Derived from partition	256/user	0
long	Longer wall times	7D	22/user;40 total	0

For all the models in this study, only 1 node has been used. However, cores upto 24 have been utilized.

Parallelization is done while submitting HFSS-IE models on supercomputer. For HFSS-IE models, 8 cores have been used parallelly and therefore, around 40GB memory is used. The

large structure runs for around 3.5 hours on supercomputer.

While running MATLAB models on supercomputer, only 1 core has been used and therefore, around 5.25GB. When S2240 is run for 26240 time-steps, it ran for 19 hours 7 minutes and 2 seconds. For S2220 and FV2420, number of time-steps was 13440. S2220 took 2 hours 25 minutes and 48 seconds while FV2420 took 10 hours 7 minutes and 2 seconds. This information is summarized in next Chapter.

Chapter 5
Results

In this chapter, the RCS results from S2220, S2240 and FV2420 schemes are compared with RCS profiles obtained from HFSS-IE MoM. Two different models are considered. In first model, simple dielectric cube is used as the scatterer. The electrical size of this structure is 0.5λ at 1 GHz. In second model, the problem is made complex by introducing concentric spheres as dielectric scatterer. The material properties of the two spheres are those of the breast tumor. The FDTD grid resolutions used are 20 and 40 cells/wavelength for S22 at 1 GHz and 10 GHz respectively for the two models. For FV24, 20 cells/wavelength at 1 GHz and 10 GHz are used respectively for the two models. Two different electrical sizes, namely 1λ and 4λ for outer sphere at 10 GHz are used for breast tumor model. In RCS comparison, ϕ is the azimuth angle and θ is the elevation angle. Fig 5.1-5.2 show the RCS comparison for cube in XY plane. Fig 5.3-5.4 show the RCS plot for cube in XZ plane and Fig 5.5-5.6 show the RCS plot for cube in YX plane.

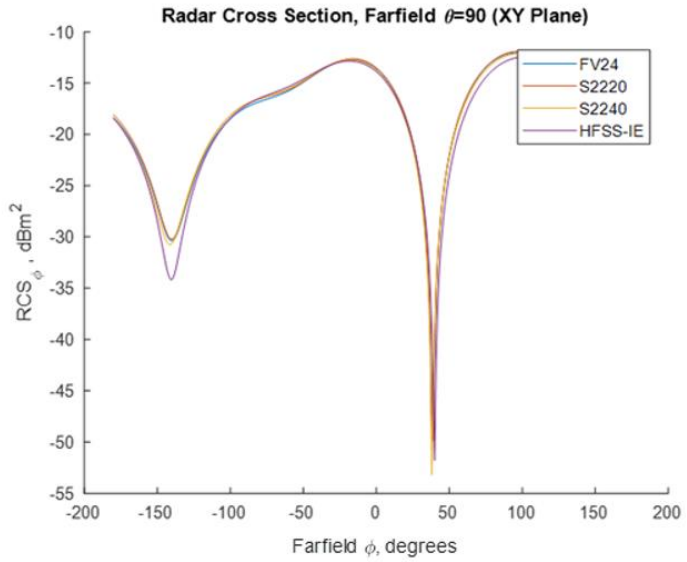

Figure 5.1: RCS$_\phi$ for XY Plane (Cube @0.5 λ @1GHz)

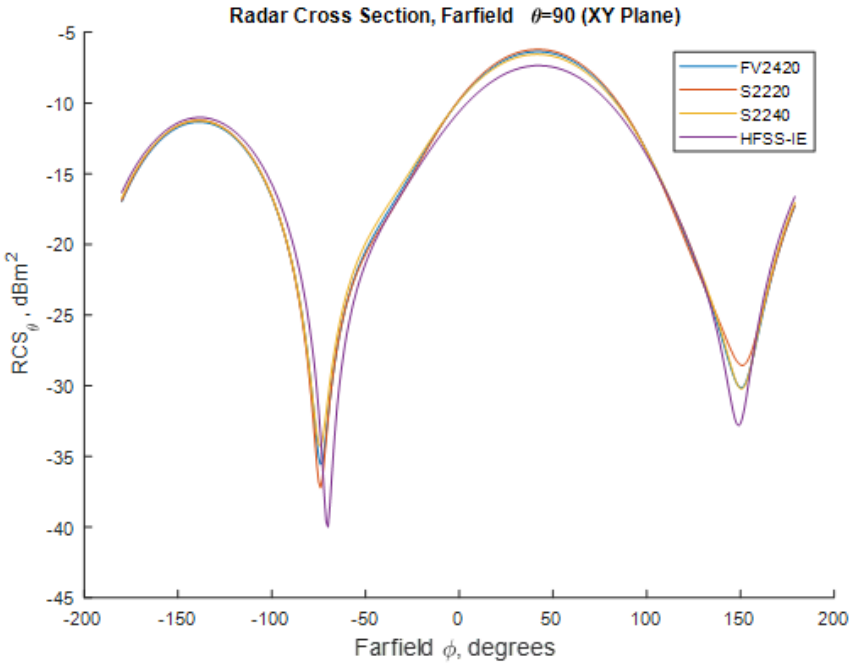

Figure 5.2: RCS_θ for XY Plane (Cube @0.5 λ @1GHz)

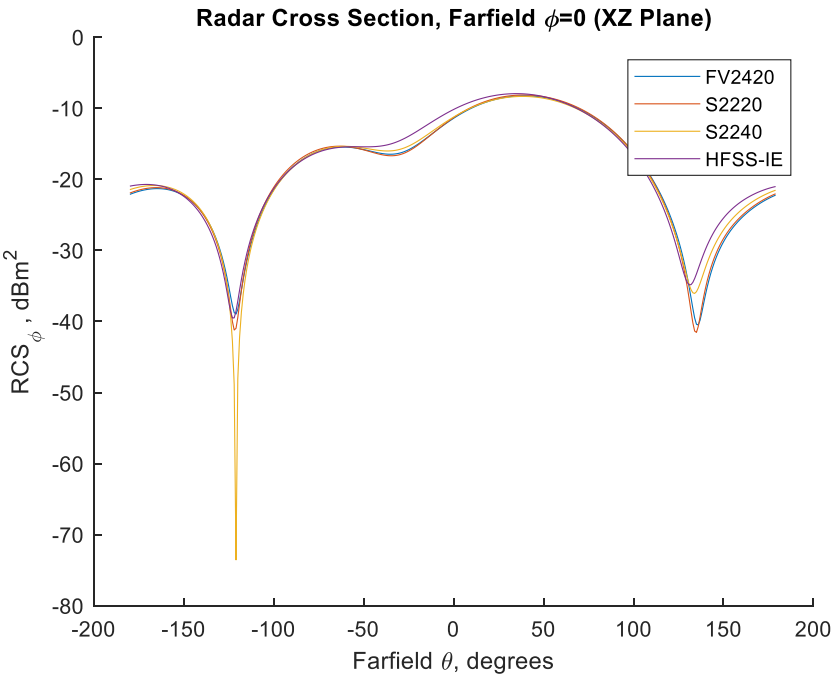

Figure 5.3: RCS_ϕ for XZ Plane (Cube @0.5 λ @1GHz)

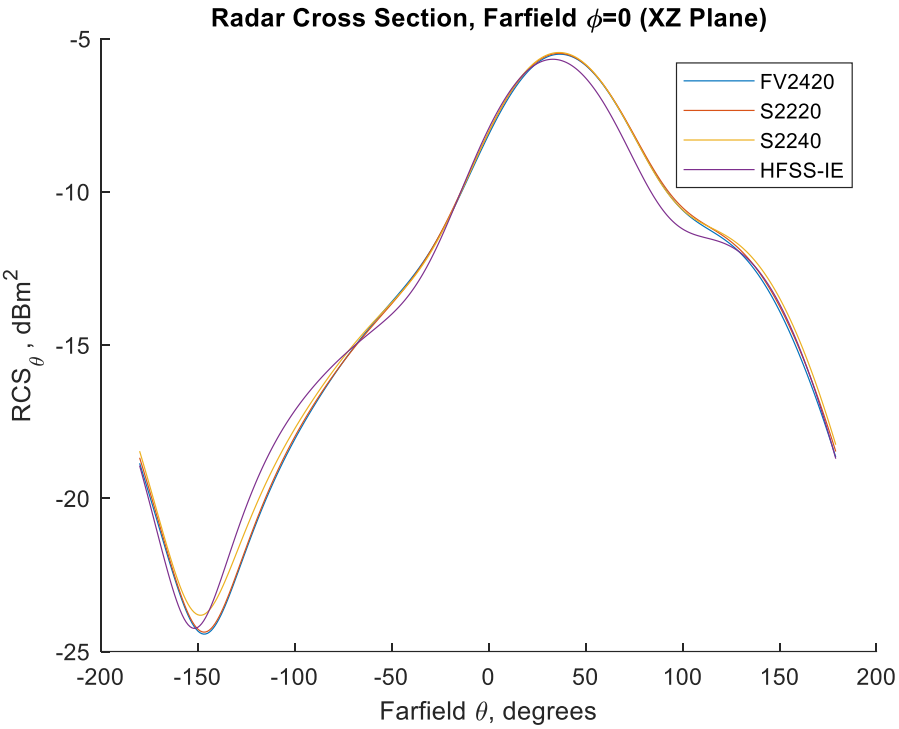

Figure 5.4: RCS_θ for XZ Plane (Cube @0.5 λ @1GHz)

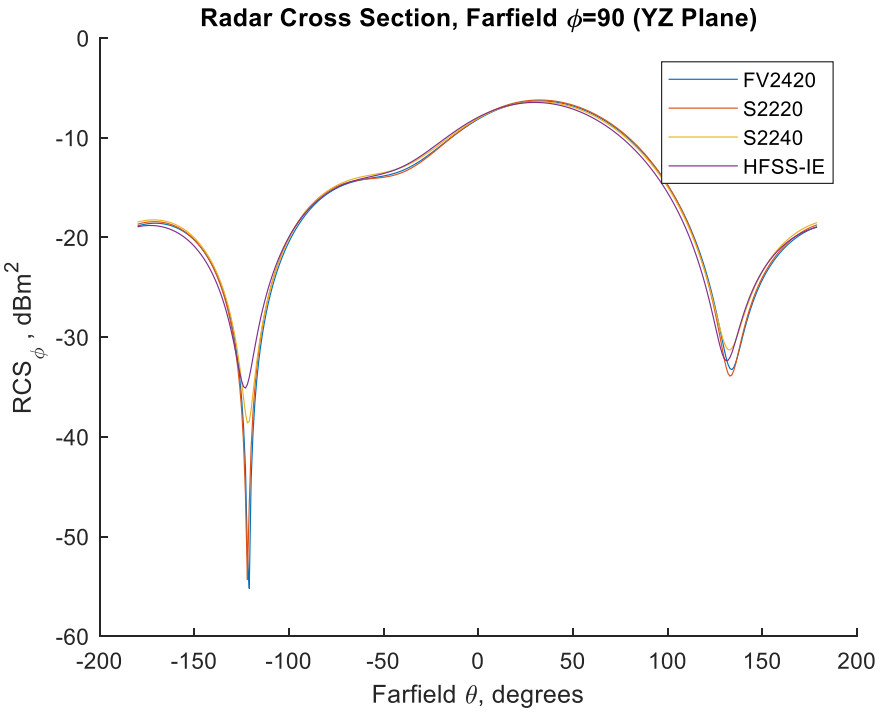

Figure 5.5: RCS_ϕ for YZ Plane (Cube @0.5 λ @1GHz)

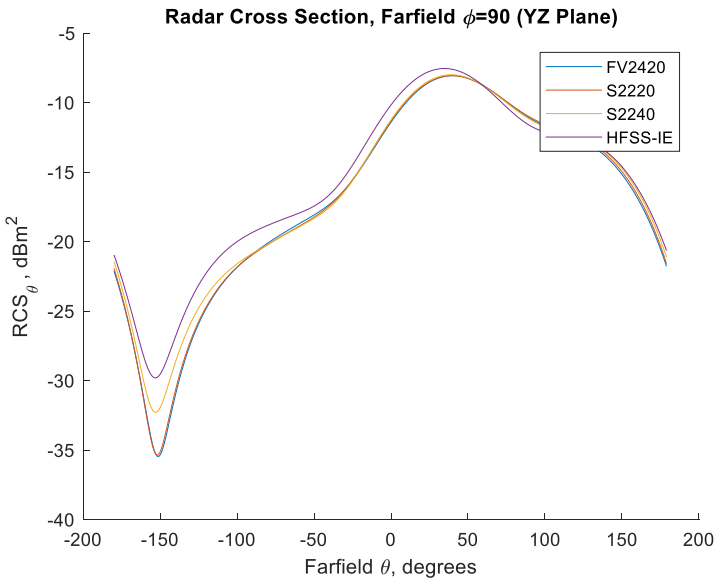

Figure 5.6: RCS_θ for YZ Plane (Cube @0.5 λ @1GHz)

Fig 5.7-5.8 show the RCS comparison for breast tumor in XY plane. Fig 5.9-5.10 show the RCS plot for breast tumor in XZ plane and Fig 5.11-5.12 show the RCS plot for breast tumor in YX plane.

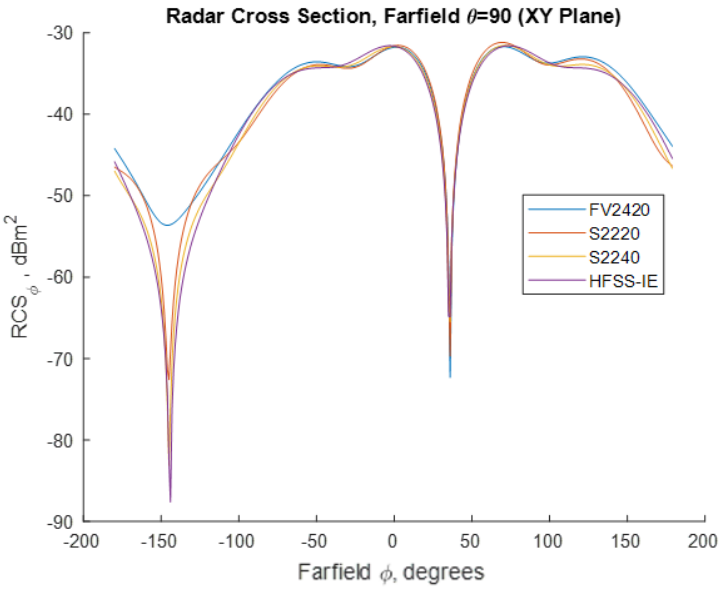

Figure 5.7: RCS_ϕ for XY Plane (breast tumor @1 λ @10 GHz)

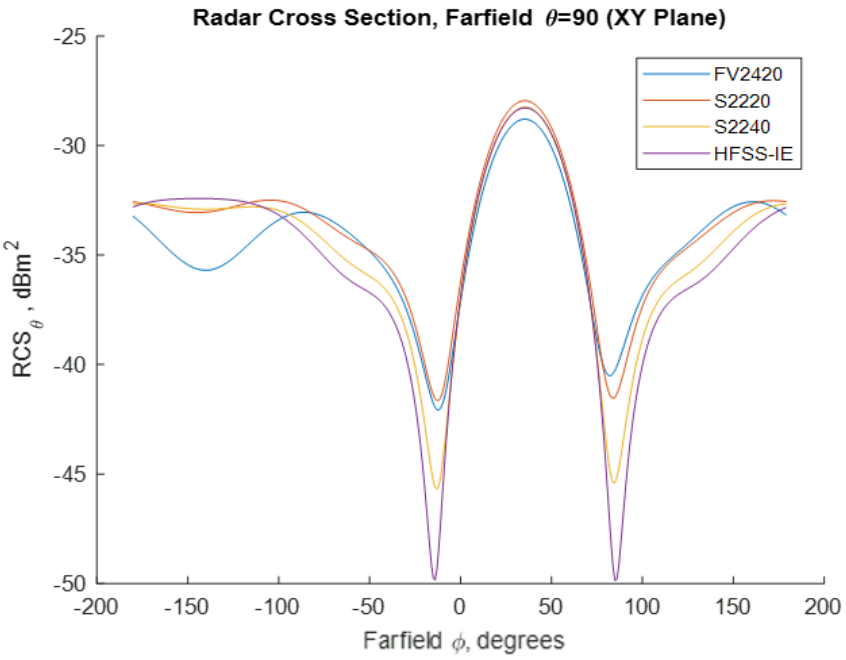

Figure 5.8: RCS_{θ} for XY Plane (breast tumor @1 λ @10 GHz)

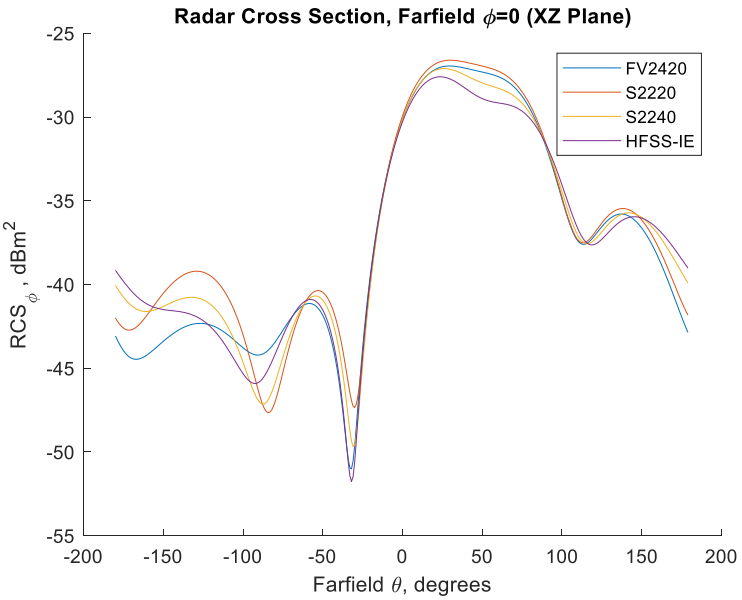

Figure 5.9: RCS_{ϕ} for XZ Plane (breast tumor @1 λ @10 GHz)

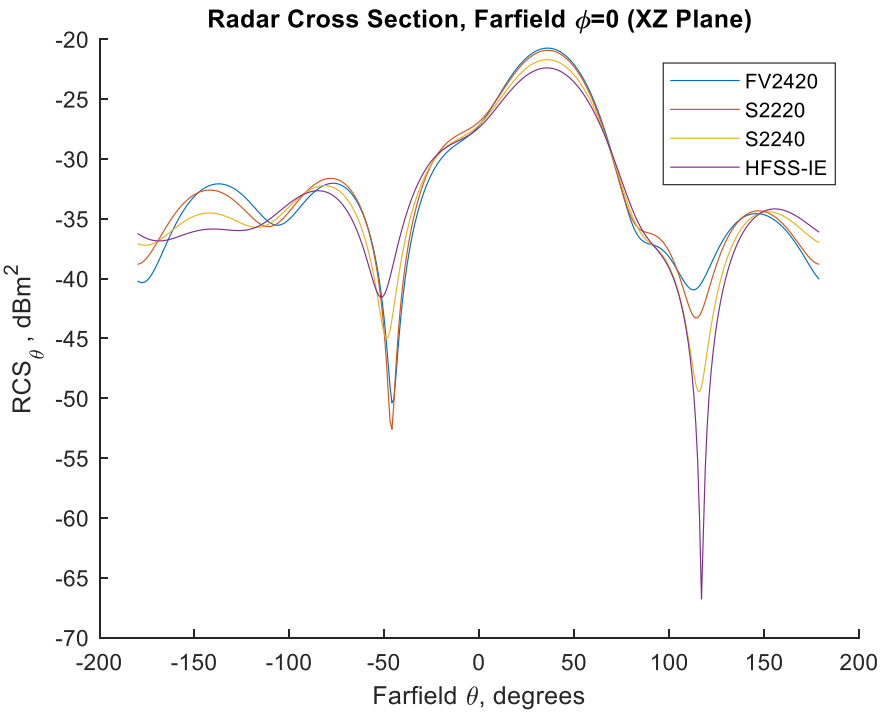

Figure 5.10: RCS_θ for XZ Plane (breast tumor @1 λ @10 GHz)

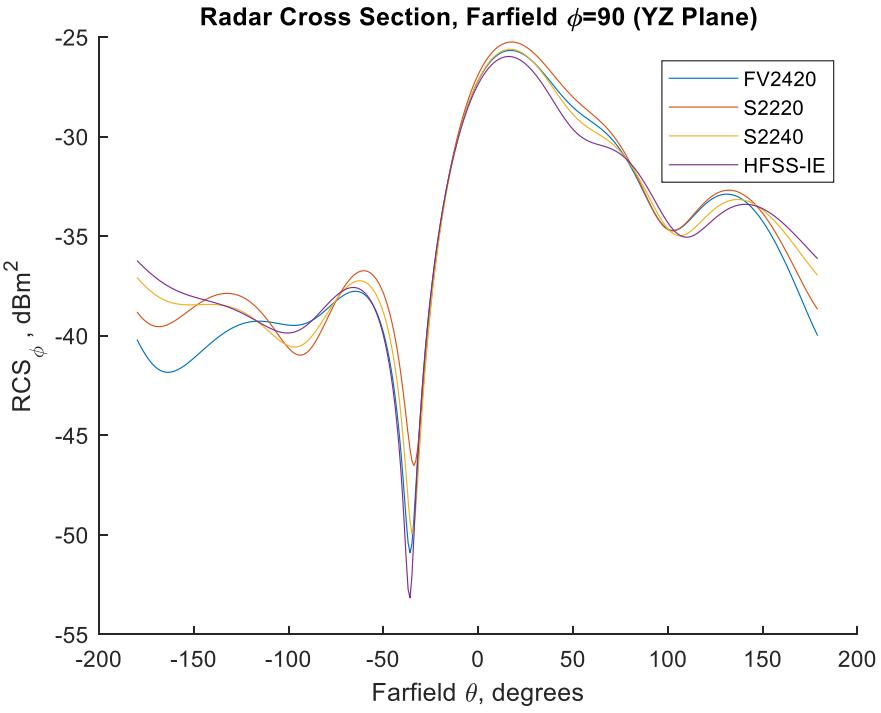

Figure 5.11: RCS_ϕ for YZ Plane (breast tumor @1 λ @10 GHz)

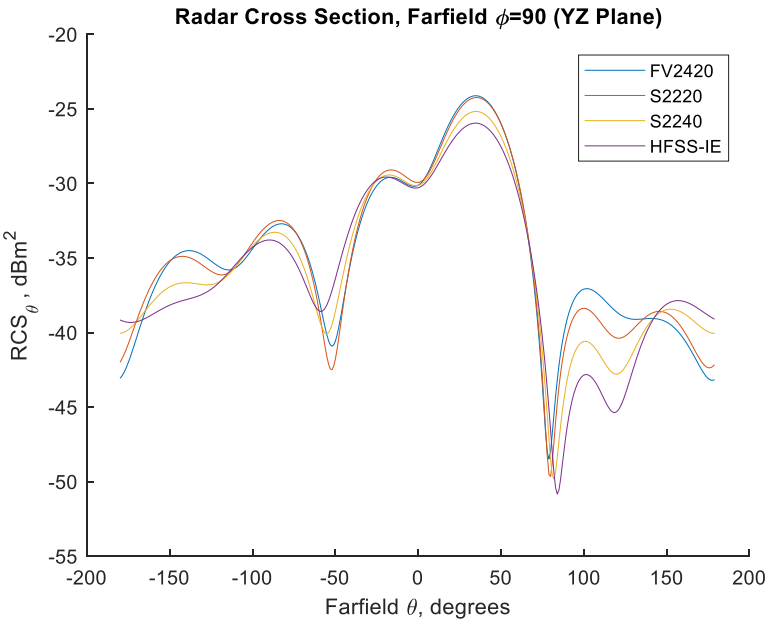

Figure 5.12: RCS_θ for YZ Plane (breast tumor @1 λ @10 GHz)

Fig 5.13-18 show the RCS plots for large structure (breast tumor). Fig 5.13-5.14 show the RCS comparison for breast tumor in XY plane. Fig 5.15-5.16 show the RCS plot for breast tumor in XZ plane and Fig 5.17-5.18 show the RCS plot for breast tumor in YX plane.

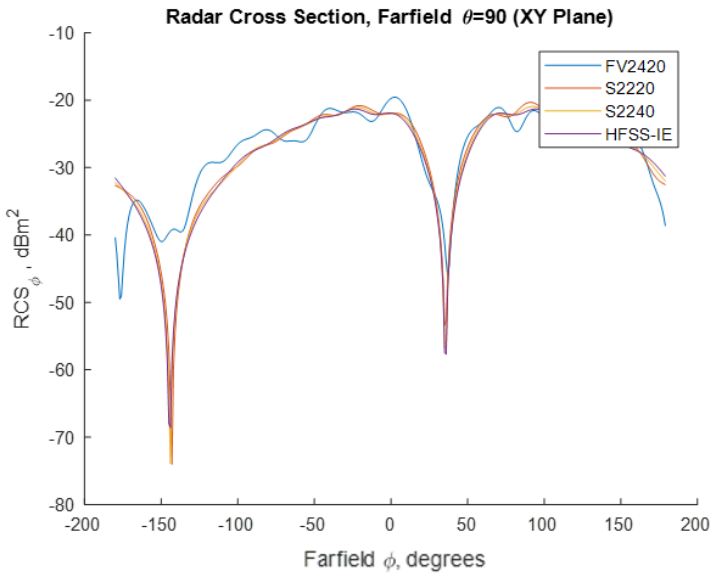

Figure 5.13: RCS_ϕ for XY Plane (breast tumor @4 λ @10 GHz)

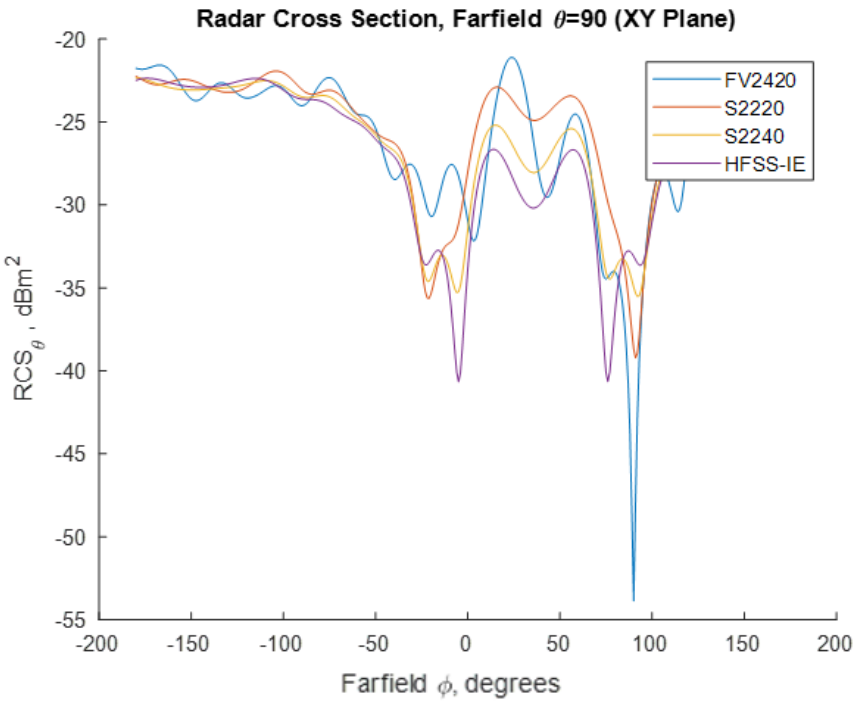

Figure 5.14: RCS_{θ} for XY Plane (breast tumor @4 λ @10 GHz)

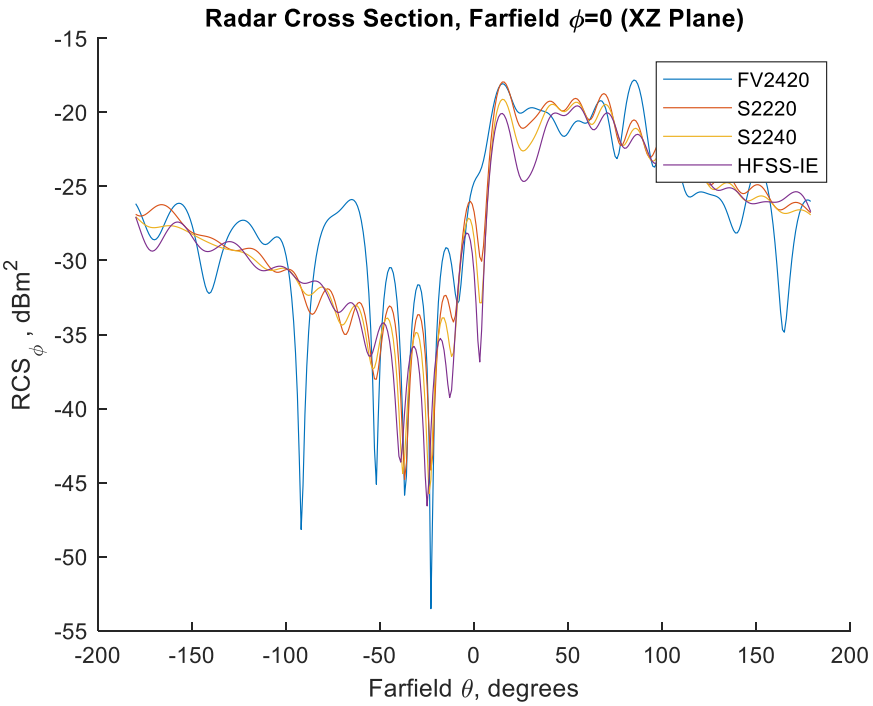

Figure 5.15: RCS_{ϕ} for XZ Plane (breast tumor @4 λ @10 GHz)

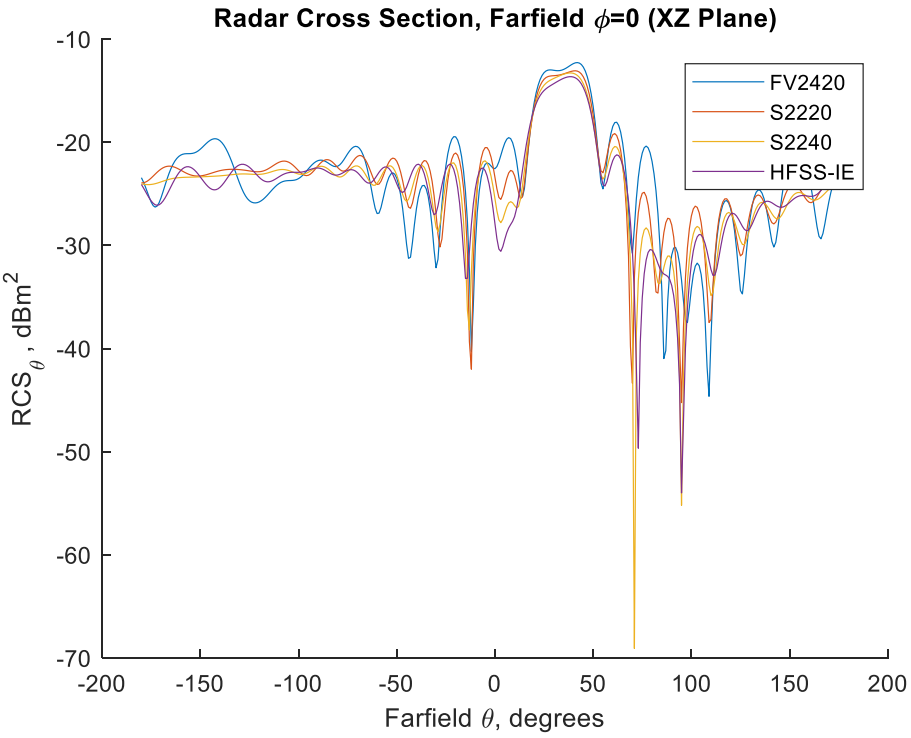

Figure 5.16: RCS$_\theta$ for XZ Plane (breast tumor @4 λ @10 GHz)

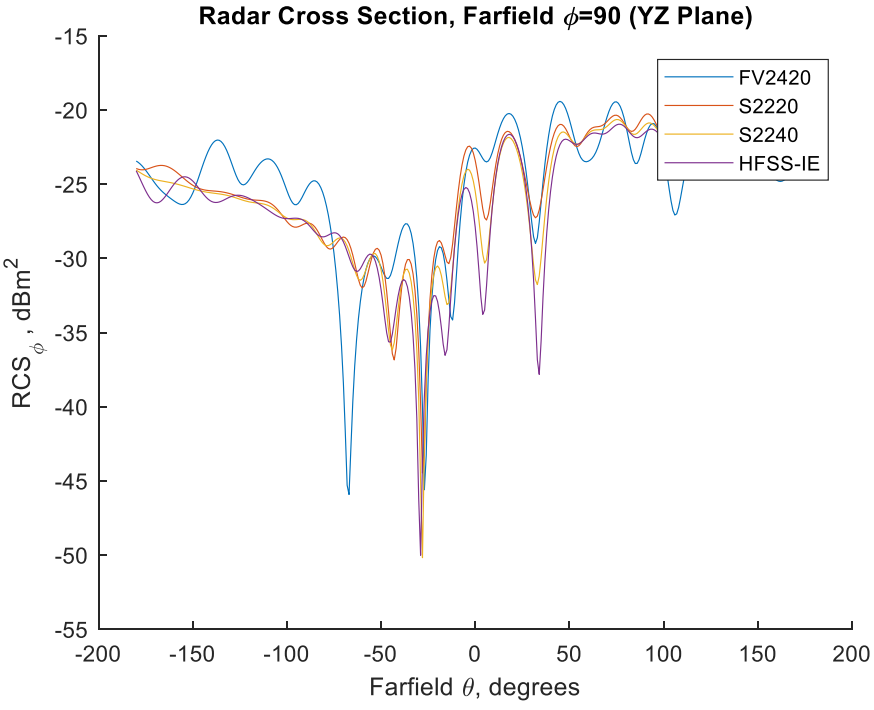

Figure 5.17: RCS$_\phi$ for YZ Plane (breast tumor @4 λ @10 GHz)

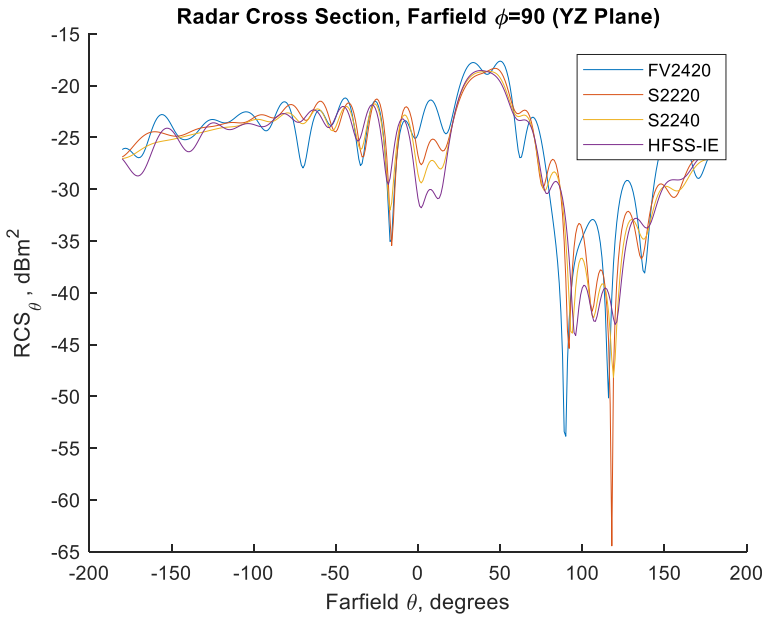

Figure 5.18: RCS_θ for YZ Plane (breast tumor @4 λ @10 GHz)

By looking at the results, it is seen that S2220 has the least accuracy on comparison with RCS of HFSS-IE. RCS plots for FV2420 and S2240 are comparable with those of HFSS-IE. For some angles in some planes, S2240 is seen to perform better than FV2420. However, overall, FV2420 has the closest match to HFSS-IE results. The convergence criterion for HFSS-IE is shown in table 5.1.

Table 5.1: HFSS-IE Convergence Criterion

Parameters	Cube	Breast Tumor
Mesh Generation (Solution Freq)	1 GHz	10 GHz
Simulation Setup (Freq)	1 GHz	10 GHz
Maximum Delta (Residual Error)	0.1	0.1
Maximum number of passes	6	6
Minimum number of passes	1	1

Parameters	Cube	Breast Tumor
Minimum converged passes	1	1
Excitation	Plane Wave	Plane Wave

Memory consumption and simulation time for MATLAB and HFSS-IE are shown in table 5.2. It is seen that the computations/time-step and net computations are greater for FV2420 compared to S2240. However, time-step size decreases as resolution increases according to Courant-Friedrichs-Lewy (CFL) Stability Criterion [16]. Therefore, the overall simulation time is lesser for FV2420 compared to S2240.

Table 5.2: Memory and simulation time for problem size $(4\lambda)^3$ (on supercomputer)

Parameters	S2240 (MATLAB)	FV2420 (MATLAB)	HFSS-IE
Memory	~5.25 GB (1 core)	~5.25 GB (1 core)	~40 GB (8 cores)
No. of time-steps	26240	13440	N/A
Computations/time-step	36	264	N/A
Net computations	944640	3548160	N/A
Total Elements	164*164*164	84*84*84	N/A
Simulation Time	~19 hours	~10 hours	~3.5 hours

Chapter 6

Conclusion

In this thesis, Material Dispersion modeling is performed in MATLAB on a Finite Volumes-Based FDTD (FV24). Radar cross-section (RCS) plots are created for FDTD at 20 cells/wavelength (S2220), 40 cells/wavelength (S2240) and for FV24 at 20 cells/wavelength. Modeling is also done in Ansys HFSS-IE and RCS plots are obtained. S2220 and S2240 results are compared against HFSS-IE results. HFSS-IE being an Integral Equation-based Method of Moments (MoM) field-solver, accurate results can be obtained.

For this work, two different models are created. The excitation for the model is a plane wave source at $\theta inc = 38.0^{o}$ and $\phi inc = 35.5^{o}$. The planewave excitation is provided using the total field/scattered field-based leakage free technique. However, for the HFSS-IE solver, the planewave arrival angles, $\theta arrival = 180 - \theta inc$ and $\phi arrival = 180 + \phi inc$ are used. The time-profile of the theta-polarized planewave is a modulated Gaussian pulse, with frequency spectrum centered around 1 GHz and 10 GHz for the two models respectively. Convolutional Perfectly Matched Layer (CPML) absorbing boundary condition is used for the models.

This work models the frequency dependence of material losses using an Auxiliary Differential Equation (ADE). To account for material dispersion, the derivation of ADE is extended for FV24 by modifying the electric field update equations. A Multi-pole Debye model, which provides an auxiliary differential equation in time domain and also produces a causal response, is used in the current analysis. This model, suitable for FDTD simulations, can simulate relative permittivity and conductivity of materials with high degree of accuracy over a wide bandwidth.

Initially, the material dispersion modeling is implemented for a simple dielectric cube. However, the cube is assumed to be of dispersive FR4 material to emulate realistic practical material model. This simple cube model is taken to test the validity and correctness of the

MATLAB code. For the cube, simulation is run for problem size of $(1\lambda)^3$ at 1 GHz. Later, the algorithm is implemented on a model consisting of two concentric spheres with material properties of that of a breast tumor. For this model, simulation is run for problem size $(1\lambda)^3$ and $(4\lambda)^3$ at 10 GHz. The large structure is taken to emulate realistic dimensions of tissue and tumor. Both MATLAB and HFSS-IE Simulations for large structure are performed on supercomputer. For the breast tumor, Cole-Cole method of material dispersion modeling is used in the literature [12]. In this work, curve-fitting using nonlinear regression is performed to obtain multi-pole Debye equivalent parameter values for the Cole-Cole model. Since the breast tumor is a practical scenario, the modeling can have biological applications. This modeling of breast tumor material can have applications in breast cancer detection and treatment.

FV24 scheme of FDTD is chosen to overcome the drawbacks of conventional FDTD. The conventional FDTD, based on second-order central difference formula, is useful only so long as the electrical size of the structure is small. Phase error accumulates in the field calculations as the dimensions of the numerical FDTD lattice become larger. The Finite Volumes-Based 3-D second-order in time, fourth-order in space (FV24) modeling is highly capable of controlling such phase errors. Therefore, it is suitable for electrically large problems at coarse grid resolutions.

The FV24 algorithm, being accurate even at coarse discretizations, provides excellent wideband performance. It is shown that keeping low number of cells per wavelength provides a substantial decrease in floating-point operations per wavelength, enabling faster computation. This fact allows significant reduction in memory usage. This feature of FV24 renders it relatively less expensive than FDTD to model three-dimensional (3-D) problems that are hundreds of wavelengths large. In this thesis, a comparison of accuracy and performance in terms of memory usage and simulation time of conventional FDTD versus FV24 is presented. To obtain better concurrency with FV2420 and HFSS-IE, the MATLAB simulation needs to be performed on much larger structures and parallelization is required.

Bibliography

[1] A. Z. Elsherbeni and V. Demir, "*The Finite-Difference Time-Domain Method for Electromagnetics with MATLAB Simulations,*" *second edition,* ACES Series on Computational Electromagnetics and Engineering, SciTech Publishing, an Imprint of IET, Edison, NJ, 2016.

[2] Ek Taflove, A., Hagness, S.: 'Computational electrodynamics: the finite-difference time-domain method' (Artech House, Boston, 2005, 3rd end.)

[3] Hadi, M.F.: 'A finite volumes-based 3-D low dispersion FDTD algorithm', IEEE Trans. Antennas Propag., 2007, 55, (8), pp. 2287- 2293.

[4] Ana Maria R Hadi, M.F., Piket-May, M.: 'A modified FDTD (2,4) scheme for modeling electrically large structures with high-phase accuracy', IEEE Trans. Antennas Propag., 1997, 45, (2), pp. 254–264.

[5] Shlager, K.L., Schneider, J.B.: 'Comparison of the dispersion properties of several low-dispersion finite-difference time-domain algorithms', IEEE Trans. Antennas Propag., 2003, 51, (3), pp. 642–653.

[6] Hadi, M.F.: 'Near-field PML optimization for low and high order FDTD algorithms using closed-form predictive equations', IEEE Trans. Antennas Propag., 2011, 59, (8), pp. 2933–2942

[7] Gibson, Nathan. (2008, October) "Approximating Dispersive Mechanisms Using the Debye Model with Distributions of Dielectric Parameters." Retrieved from http://math.oregonstate.edu/~math_reu/proceedings/REU_Proceedings/Proceedings2008/2008 Barrese_Chugh.pdf

[8] R. C. Bollimuntha, M. F. Hadi, M. J. Piket-May and A. Z. Elsherbeni, "Dispersion optimized plane wave sources for scattering analysis with integral based high order finite difference time domain methods," in IET Microwaves, Antennas & Propagation, vol. 10, no. 9, pp. 976-982, 6 18 2016.

[9] T. Tan and M. Potter, "1–D multipoint auxiliary source propagator for the total/field/scattered-field FDTD formulation," IEEE Antennas and Wireless Propagation Letters, vol. 6, pp. 144–148, 2007.

[10] T. Martin, “An improved near- to far-zone transformation for the finite-difference time-domain method,” IEEE Transactions on Antennas

[11] C. A. Balanis, Advanced Engineering Electromagnetics. New York: John Wiley, 1989.

[12] M. Lazebnik, D. Popovic, L. McCartney, C. B.Watkins, M.J. Lindstrom, J. Harter, S. Sewall, T.Ogilvie, A. Magliocco, T. M. Breslin,W. Temple, D. Mew, J. H. Booske, M. Okoniewski and S. C. Hagness, “A large-scale study of the ultrawideband microwave dielectric properties of normal, benign and malignant breast tissues obtained from cancer surgeries”, 2007 Phys. Med. Biol. 52.

[13] M. El-Shenawee and E. L. Miller, "Spherical harmonics microwave algorithm for shape and location reconstruction of breast cancer tumor," in IEEE Transactions on Medical Imaging, vol. 25, no. 10, pp. 1258-1271, Oct. 2006

[14] RCTraining (2018, May 7). ResearchComputing/Research-Computing-User-Tutorials. Retrieved from https://www.colorado.edu/rc/

[15] K. S. Yee, “Numerical solution of initial boundary value problems involving Maxwell’s equations in isotropic media,” IEEE Transactions on Antennas and Propagation, vol. 14, pp. 302–307, 1966.

[16] R. Courant, K. Friedrichs, and H. Lewy, “On the partial difference equations of mathematical physics,” IBM Journal of Research and Development, vol. 11, no. 2, pp. 215–234, 1967.

[17] M. M. Okoniewski, M. P. Mrozowski, and M. A. Stuchly, “Simple treatment of multi-term dispersion in FDTD,” IEEE Microwave and Guided Wave Letters, vol. 7, no. 5, pp. 121–123, 1997.

[18] R. J. Luebbers, K. S. Kunz, M. Schnizer, and F. Hunsberger, “A finite-difference time-domain near zone to far zone transformation,” IEEE Transactions on Antennas and Propagation, vol. 39, no. 4, pp. 429–433, 1991.

[19] R. J. Luebbers, D. Ryan, and J. Beggs, “A two dimensional time domain near zone to far zone transformation,” IEEE Transactions on Antennas and Propagation, vol. 40, no. 7, pp. 848–851, 1992.

[20]S. A. Schelkunoff, “Some equivalence theorem of electromagnetics and their application to radiation problem,” Bell System Technical Journal, vol. 15, pp. 92–112, 1936.

[21] C. A. Balanis, Antenna Theory: Analysis and Design, 3rd edn. Hoboken, NJ: John Wiley & Sons, 2005.

[22]J. Roden and S. Gedney, “Convolution PML (CPML): an efficient FDTD implementation of the CFS-PML for arbitrary media,” Microwave and Optical Technology Letters, vol. 27, no. 5, pp. 334–339, 2000.